The Mediterranean forecasting system.
Part I: evolution and performance

Giovanni Coppini[1,*], Emanuela Clementi[2], Gianpiero Cossarini[3], Stefano Salon[3], Gerasimos Korres[4] , Michalis Ravdas[4], Rita Lecci[1], Jenny Pistoia[2], Anna Chiara Goglio[2], Massimiliano Drudi[1], Alessandro Grandi[1], Ali Aydogdu[2], Romain Escudier[2,5], Andrea Cipollone[2], Vladislav Lyubartsev[1], Antonio Mariani[1], Sergio Cretì[1], Francesco Palermo[1], Matteo Scuro[1], Simona Masina[2], Nadia Pinardi[6,7], Antonio Navarra[6,8], Damiano Delrosso[9], Anna Teruzzi[3], Valeria Di Biagio[3], Giorgio Bolzon[3], Laura Feudale[3], Gianluca Coidessa[3], Carolina Amadio[3], Alberto Brosich[3], Arnau Miró[10], Eva Alvarez[3], Paolo Lazzari[3], Cosimo Solidoro[3], Charikleia Oikonomou[4], Anna Zacharioudaki[4]

[1] Ocean Predictions and Applications Division, Fondazione Centro Euro-Mediterraneo sui Cambiamenti Climatici (CMCC), Italy
[2] Ocean Modeling and Data Assimilation Division, Centro Euro-Mediterraneo sui Cambiamenti Climatici (CMCC), Italy
[3] Istituto Nazionale di Oceanografia e di Geofisica Sperimentale (OGS), Italy
[4] Hellenic Centre for Marine Research (HCMR), Greece
[5] Mercator Océan International, France
[6] Centro Euro-Mediterraneo sui Cambiamenti Climatici (CMCC), Bologna, Italy
[7] Department of Physics and Astronomy, Università di Bologna, Bologna, Italy
[8] Department of Biological, Geological and Environmental Sciences (BIGEA), Università di Bologna, Bologna, Italy
[9] Istituto Nazionale di Geofisica e Vulcanologia (INGV), Italy
[10] Barcelona Supercomputing Center, Barcelona (BSC), Spain

Correspondence to: Giovanni Coppini giovanni.coppini@cmcc.it

Abstract. The Mediterranean Forecasting System produces operational analyses, reanalyses and 10-day forecasts for many Essential Ocean Variables (EOVs), from currents, temperature, salinity, sea level to wind waves and pelagic biogeochemistry. The products are available at a horizontal resolution of 1/24 degrees (approximately 4 km) and 141 unevenly spaced vertical levels.

The core of the Mediterranean Forecasting System is constituted by the physical (PHY), the biogeochemical (BIO) and the wave (WAV) components, consisting of both numerical models and data assimilation modules. The 3 components together constitute the so-called Mediterranean Monitoring and Forecasting Center (Med-MFC) of the Copernicus Marine Service. Daily 10-day forecasts are produced by the PHY, BIO and WAV operational systems as well as analyses, while reanalyses are produced for the past 30 years about every ~3 years and extended (yearly). The modelling systems, their coupling strategy and evolutions are illustrated in detail. For the first time, the quality of the products are documented in terms of skill metrics evaluated on a common three-year period (2018-2020), giving the first complete assessment of uncertainties for all the Mediterranean environmental variable analyses.

1 Introduction

Ocean analysis and forecasting systems are now available for the global and world ocean regional seas at different spatial scales and with different numbers of Essential Ocean Variables (EOV) considered (Tonani et al., 2015). The societal drivers for the operational products stemming out of the ocean analysis and forecasting products are the safety of maritime transport, multiple coastal hazards and climate anomalies. Moreover, the operational products are at the basis of new understanding of the dynamics of the ocean circulation (Pinardi et al., 2015), its linked biogeochemical cycles, among others, carbon uptake and eutrophication (Melaku Kanu et al., 2015; von Schuckmann et al., 2020) and extreme storm surge events (Giesen et al., 2021). The ocean analysis and forecasting system for the entire Mediterranean Sea was set up in the past 15 years (Pinardi and Coppini, 2010; Pinardi et al., 2017; Lazzari et al., 2010; Salon et al., 2019; Ravdas et al., 2018; Katsafados et al., 2016) and in 2015 it became operational in the framework of the Copernicus Marine Service which is the marine component of the Copernicus Programme European Union service for a sustainable use of the ocean providing free, regular and systematic information on the state of the Blue (physical), White (sea ice) and Green (biogeochemical) ocean on the global and regional scales. The Copernicus Marine service in Europe has shown the strength of a state-of-the-art operational service implemented by hundreds of experts and teams, distributed throughout Europe, coming from public and private sectors, from operational and research organisations, from different countries, from diverse cultures and relations to the ocean (Le Traon et al., 2017; Alvarez Fanjul et al., 2022). In this paper we give an overview of the "core" components of the system, i.e., the numerical models and the data assimilation modules that represent the eddy-resolving ocean general circulation, the biogeochemical tracers and the wind waves. Furthermore, we will document the quality of EOV products using goodness indices (Brassington et al., 2017). The core components constitute the so-called Mediterranean Monitoring and Forecasting Center (Med-MFC) of Copernicus Marine Service (Le Traon et al., 2019). The integrated approach of the Med-MFC system represents a unique opportunity for the users to access state-of-the-art information provided in a uniform manner (e.g., same grid, unique format, unique point of access). This ocean analysis and forecasting system, hereafter Med-MFC, produces analyses, 10 days forecasts and reanalysis (Adani et al., 2011; Pinardi et al., 2015; von Schuckmann et al., 2016; von Schuckmann et al., 2018; von Schuckmann et al., 2019; Terzic et al., 2021; Simoncelli et al., 2016; Simoncelli et al., 2019; Ravdas et al., 2018, Escudier et al., 2020; Escudier et al., 2021, Cossarini et al., 2021).

An essential task of the production activities concerns the continuous assessment of the quality of the products (Sotillo et al., 2021; Alvarez Fanjul et al., 2022) which is achieved at two levels: (i) the pre-qualification of the systems before delivering a new release, including an extensive scientific validation of the products, published in the QUality Information Documents (QUIDs) available on the Copernicus Marine Product Catalogue; (ii) the operational evaluation of the skill metrics during operations, made available through the Copernicus Marine Product Quality Dashboard Website (https://pqd.mercator-ocean.fr), as well as through the Mediterranean regional validation websites implemented at the level of the Med-MFC production units (PHY: https://medfs.cmcc.it/, WAV: http://Med-MFC-wav.hcmr.gr/ , BIO: www.medeaf.ogs.it/NRT-

66 validation). All the delivered variables are thus validated with respect to satellite and in-situ observations using Copernicus
67 Marine observational datasets, as well as additional datasets, climatologies or literature information when needed.
68 The Mediterranean Sea is a semi-enclosed basin with an anti-estuarine circulation corresponding to a 0.9/0.8 ±0.06 Sv
69 baroclinic inflow/outflow at the Strait of Gibraltar, positive energy inputs by the winds and a net buoyancy losses inducing a
70 vigorous overturning circulation (Cessi et al., 2014; Pinardi et al., 2019). The basin scale circulation is dominated by mesoscale
71 and sub-mesoscales variability (Pinardi et al., 2016; Bergamasco et al., 2010; Pinardi et al., 2006; Robinson et al., 2001; Ayoub
72 et al., 1998), the former subdivided into semi-permanent and synoptic mesoscales with a spatial scale larger than 4-6 times the
73 local Rossby radius of deformation. The stratification is large during summer in the first 50 meters and during winter the water
74 column is practically unstratified. The Mediterranean Sea is an oligotrophic basin (Siokou-Frangou et al., 2010) with a west-
75 to-east decreasing productivity gradient (Lazzari et al., 2012) and relatively high primary productivity in open ocean areas
76 where winter mixing increases surface nutrients (Cossarini et al., 2019). The wave conditions are driven by the winter
77 storminess, while summer is characterised by low significant wave height values and higher value scatter (Ravdas et al., 2018).
78 The yearly mean wave period, as estimated from available wave buoys over the Mediterranean Sea, amounts to 3.82 s with
79 typical deviations of 0.92 s, while the mean significant wave height is 0.82 m (1.28 m as estimated by satellite observations)
80 with typical deviations of 0.67 m (0.77 m for satellite data).
81 In this paper we describe the final set up of the Med-MFC core components for the period 2017-2020: The Med-MFC
82 modelling systems share the same grid resolution (1/24°), bathymetry and use the same atmospheric and river forcing fields.
83 Moreover, daily mean fields evaluated by the physical model are used to force the wave component (surface currents) and the
84 transport-biogeochemical model (temperature, salinity, horizontal and vertical velocities, sea level, diffusivity). This allows
85 several model parametrizations to be calibrated to obtain the best result in term of the specific environmental variable
86 considered by each component. In the Copernicus Marine Service the approach of forcing waves and biogeochemistry models
87 with information from the hydrodynamic models is used and represents a standard which is also applied for the other MFCs.
88 Several MFCs also the online coupling between physics and waves models and between physics and biogeochemical models.
89 Furthermore, this weakly coupled system ensures an efficient development of the data assimilation modules connected to each
90 numerical model modules and specific input data sets. It is a distributed system that shares information when and how it is
91 required by relevant processes, with efficiency and effectiveness. Due its rather unique structure and the quality of its products
92 the system described could be used as a basic standard for new systems to be developed.
93 The paper is organised as follows. Section 2 overviews the technical specifications of the Med-MFC components, Section 3
94 describes the quality of the system for a reference period from 2018 to 2020 and of the forcing, Section 4 concludes the paper
95 and presents future perspectives.

2. Description of the Med-MFC core components

The structure of the Med-MFC core components is shown in Figure 1: the physical component (PHY) is composed of the NEMO general circulation model (Madec et al., 2019) coupled to the WaveWatch-III (WW3) wave model (Clementi et al., 2017a) and the ocean data assimilation OceanVar 3DVAR (Dobricic and Pinardi, 2008 and Storto et al., 2015); the biogeochemical component (BIO) is composed of the Biogeochemical Flux Model (BFM), the tracer transport (OGSTM) and a data assimilation scheme (Lazzari et al., 2012; Lazzari et al., 2016; Cossarini et al., 2015; Vichi et al., 2020), forced daily by the daily mean of the PHY component fields; the wave component (WAV) is composed of the wave model WAM (WAMDI Group, 1988) and its assimilation scheme, forced daily by the daily mean of the PHY component fields. Daily 10 days forecasts are produced with all PHY, BIO and WAVE components as well as analyses and reanalyses as described below.

Each component of the Med-MFC has its own data assimilation system, so that important effort was made to extract the most relevant information from satellite and in- situ observations to produce analysis and correct initial conditions for the forecast in order to benefit the forecasting skills. The main goal of the paper is to present the current quality of the operational system components by comparing the analysis and - for specific variables, such as significant wave height - the background (simulation) with observations, in-situ and/or satellites. The skill of the wave and biogeochemical models is assessed by considering inter-comparisons of the model solution during the 24-h analysis phase with in-situ and remotely sensed observations. As the latter are ingested into the model through data assimilation, the first guess model fields (i.e. model background) are used instead of analyses.

2.1. The general circulation model component

2.1.1. Numerical model description

The PHY numerical model component comprises a two-way coupled current-wave model based on NEMO and WW3 implemented over the whole Mediterranean basin and extended into the Atlantic Sea in order to better resolve the exchanges with the Atlantic Ocean (Figure 2). The model horizontal grid resolution is 1/24° (ca. 4 km) and is resolved along 141 unevenly spaced vertical levels (Clementi et al., 2017b; Clementi et al., 2019). The topography is an interpolation of the GEBCO 30 arc second grid (Weatherall et al., 2015) filtered and specifically modified in critical areas such as: the Eastern Adriatic coastal areas (to avoid instabilities in circulation due to the presence of a large number of small islands), Gibraltar and Messina straits (to better represent the transports), Atlantic edges external border (to avoid large bathymetric inconsistencies with respect to the Copernicus Global Analysis and Forecast product in which the model is nested). All the numerical model choices are documented in Table A1.

The general circulation model considers the non-linear free surface formulation and vertical z-star coordinates. The numerical scheme uses the time-splitting formulation to solve the free surface and the barotropic equations with a (100 times) smaller time step with respect to the one used to evaluate the prognostic 3D variables (240 seconds). The active tracers (temperature and salinity) advection scheme is a mixed up-stream/MUSCL (Monotonic Upwind Scheme for Conservation Laws; Levy et

128 al., 2001) as modified in Oddo et al. (2009). The vertical diffusion and viscosity terms are defined as a function of the
129 Richardson number, following Pacanowski and Philander (1981). The air-sea surface fluxes of momentum, mass, and heat are
130 computed using bulk formulae described in Pettenuzzo et al. (2010) and the Copernicus satellite gridded SST data (Buongiorno
131 Nardelli et al., 2013) is used to correct the non-solar heat flux using a relaxation constant of 110 $Wm^{-2}K^{-1}$ centred at midnight.
132 A detailed description of other specific features of the model implementations can be found in Tonani et al. (2008), Oddo et
133 al. (2009) and Oddo et al. (2014).

134 The wave model WW3 is discretized by means of 24 directional bins (15° resolution) and 30 frequency bins (ranging between
135 0.05 Hz and 0.7931 Hz) to represent the wave spectral distribution. The wave model is implemented using the same bathymetry
136 and grid of the hydrodynamic model and uses the surface currents to evaluate the wave refraction but assumes no interactions
137 with the ocean bottom. The Mediterranean implementation of WW3 follows WAM cycle4 model physics (Gunter et al., 1993);
138 the wind input and dissipation terms are based on Janssen's quasi-linear theory for wind-wave generation (Jansen, 1989;
139 Jansen, 1991), the wave dissipation term is based on Hasselmann (1974) whitecapping theory according to Komen et al. (1984)
140 and the non-linear wave-wave interaction is modelled using the Discrete Interaction Approximation (DIA, Hasselmann et al.,
141 1985). The exchanges between the circulation and wave models are performed using an online two-way coupling between
142 NEMO and WW3. The models are forced by the same atmospheric fields (high resolution ECMWF analysis and forecast
143 winds) and are two-way coupled at hourly intervals exchanging the following fields: NEMO sends to WW3 the sea surface
144 currents and temperature which are then used to evaluate the wave refraction and the wind speed stability parameter,
145 respectively. The neutral drag coefficient computed by WW3 is passed to NEMO to compute the surface wind stress.

146 The NEMO-WW3 coupled system is intended to provide the representation of current-wave interaction processes in the ocean
147 general circulation. At the moment the feedback is considered only for the surface wind stress drag coefficient and more details
148 on this wave-current model coupling can be found in Clementi et al. (2017a).

149 **2.1.2. Model initialization, external forcing and boundary conditions**

150 The PHY component was initialised in January 2015 using temperature and salinity winter climatological fields from WOA13
151 V2 (World Ocean Atlas 2013 V2, https://www.nodc.noaa.gov/OC5/woa13/woa13data.html). The atmospheric forcing fields
152 for both NEMO and WW3 models are from the 1/8° horizontal resolution at 6 hours temporal frequency (3 hours frequency is
153 used to force the first 3 days of forecast) operational analysis fields from the European Centre for Medium-Range Weather
154 Forecast (ECMWF) Integrated Forecasting System (IFS) and a higher spatial resolution of 1/10° (with higher forecast temporal
155 frequency of 1-3-6 hours according to the forecast leading time) is used starting from year 2020.

156 The circulation model's lateral open boundary conditions (LOBC) in the Atlantic Ocean are provided by the Copernicus Global
157 Analysis and Forecast product (Lellouche et al., 2018) at 1/12° horizontal resolution and 50 vertical levels. Daily mean fields
158 are used, and the numerical schemes applied at the open boundaries are the Flather (1976) radiation scheme for the barotropic
159 velocity and the Orlanski (1976) radiation condition (normal projection of oblique radiation case) with adaptive nudging
160 (Marchesiello et al., 2001) for the baroclinic velocity and the tracers. The nesting technique is detailed in Oddo et al. (2009),

161   who also show a marked improvement in the salinity characteristics of the Modified Atlantic Water and in the Mediterranean

162   sea level seasonal variability. The Dardanelles Strait boundary conditions (Delrosso, 2020) consist of a merge between the

163   Copernicus global ocean products and daily climatology derived from a Marmara Sea box model (Maderich et al., 2015). The

164   WW3 model implementation considers closed boundaries in both Atlantic Ocean and Dardanelles strait.

165   The river runoff inputs consist of monthly climatological data for 39 major rivers (characterized by an average discharge larger

166   than 50 m^3/s) with a prescribed constant salinity at river mouth (Delrosso, 2020) evaluated by means of sensitivity experiments

167   and listed in Table A.4. More realistic and time varying river salinity values (at least for major rivers) will be evaluated in

168   future modeling evolutions using an estuary box model, such as the one presented in Verri et al. (2020), coupled to the

169   hydrodynamic model.

2.1.3 The data assimilation component

171   A 3D-variational data assimilation scheme, called OceanVar, initially developed by Dobricic and Pinardi (2008) and further

172   improved for a wide range of ocean data assimilation applications (Storto et al., 2015) is coupled to NEMO.

173   The OceanVar scheme aims to minimise the cost function as described in the following Eq. (1):

$$J = \frac{1}{2}\delta x^T B^{-1}\delta x + \frac{1}{2}(H\delta x - d)^T R^{-1}(H\delta x - d), \tag{1}$$

177   where $\delta x = x - x_b$, and x is the unknown ocean state, equal to the analysis x_a at the minimum of J, x_b is the background state,

178   $d = y - H(x_b)$ is the misfit between an observation y and its modelled correspondent mapped onto the observation space to

179   the observation location by the observation operator, H.

180   In OceanVar, the background error covariance matrix is considered as $B = VV^T$, where V is a sequence of linear operators:

181   $V = V_\eta V_H V_V$. Multivariate EOFs (Empirical Orthogonal Functions, described in Dobricic et al., 2006 and Pistoia et al., 2017)

182   compose the vertical component operator, V_V. EOFs are computed in every grid point for the sea surface height, temperature

183   and salinity using a three-year simulation in order to capture the mesoscale eddy variability that is assumed to represent the

184   unbalanced component of the background error covariance. The horizontal covariances, V_H, are modelled by an iterative

185   recursive filter (Dobric and Pinardi, 2008; Storto et al., 2014). In order to assimilate altimeter observations, the dynamic height

186   operator, V_η, developed in Storto et al. (2011) is used. A reference level of 1000 m is used for this operator so SLA along track

187   observations over water shallower than this depth are not assimilated.

188   The observational error covariance matrix, R, is estimated following Desroziers et al. (2005) relationship. The assimilated

189   observations include along-track altimeter sea level anomaly from six satellites and in-situ vertical temperature and salinity

190   profiles from Argo floats. The SLA tracks provided by nadir altimeters are assimilated by subsampling every second

191   observation to reduce the spatial correlation between consecutive measurements. A special quality control procedure is applied

192   to real-time Argo data before they are assimilated. It consists of removing real-time profiles with negative temperature and/or

193   salinity, temperature higher than 45° C and salinity higher than 45 PSU, removing profiles with gaps in the observations of
194   more than 40 m in the first 300 m depth (to avoid possible inconsistencies in the thermocline), profiles with observations
195   provided only below 35 m depth and observations in the 1st model layer (0-2 m). Moreover, a background quality check is
196   implemented to reject observations whose square departure exceeds the sum of the observational and background-error
197   variances 64 times in case of SLA and 25 times in case of in-situ temperature and salinity. The quality checks are applied to
198   each individual observation of each Argo vertical profile and for each altimeter track. The misfits are computed at the
199   observation time by applying the FGAT (First Guess at the Appropriate Time) procedure and the corrections to the background
200   are applied once a day to the restart file using observations within a one-day time window.

201   **2.2. The wind wave component**

202   **2.2.1. Numerical model description**

203   The WAV component consists of two nested wave model implementations: the first grid covers the whole Mediterranean Sea
204   at 1/24° horizontal resolution and it is nested within a coarser resolution wave model grid at 1/6° horizontal resolution
205   implemented over the Atlantic Ocean (Figure 2).
206   The wave model is based on the state-of-the-art third generation WAM Cycle 4.6.2 which is a modernised and improved
207   version of the well-known and extensively used WAM Cycle 4 wave model (WAMDI Group, 1988; Komen at al., 1994).
208   WAM solves the wave transport equation explicitly without any presumption on the shape of the wave spectrum. Its source
209   terms include the wind input, whitecapping dissipation, nonlinear transfer, and bottom friction. The wind input term is adopted
210   from Snyder et al. (1981). The whitecapping dissipation term is based on Hasselman (1974) whitecapping theory. The wind
211   input and whitecapping dissipation source terms of the present cycle of the wave model are a further development based on
212   Janssen´s quasi-linear theory of wind-wave generation (Jansen, 1989; Jansen, 1991). The nonlinear transfer term is a
213   parameterization of the exact nonlinear interactions (Komen et al., 1984 and Hasselman et al., 1985). Lastly, the bottom friction
214   term is based on the empirical JONSWAP model of Hasselman et al. (1973).
215   The bathymetric map has been constructed using the GEBCO 30arc-second bathymetric data set for the Mediterranean Sea
216   model and the ETOPO 2 data set (U.S. Department of Commerce, National Oceanic and Atmospheric Administration, National
217   Geophysical Data Centre, 2006. 2-minute Gridded Global Relief Data) for the North Atlantic model. In both cases mapping
218   on the model grid was done using bi-linear interpolation accompanied by some degree of isotropic Laplacian smoothing. This
219   bathymetry is different from the one used for the PHY component, optimized for the specific quality of the wave products.
220   The wave spectrum is discretized using 32 frequencies, which cover a logarithmically scaled frequency band from 0.04177 Hz
221   to 0.8018 Hz (covering wave periods ranging from approximately 1 s to 24 s) at intervals of $df/f = 0.1$ and 24 equally spaced
222   directions (15 degrees bin). The WAV model component runs in shallow water mode considering wave refraction due to depth
223   and currents in addition to depth-induced wave breaking. Modifications from default values of WAM 4.6.2 have been
224   performed in the input source functions as a result of a tuning procedure. Specifically, the value of the wave age shift parameter

225   (ZALP) in the wind input source function was set to 0.011 (0.008 is the default) for the Mediterranean model and the tunable

226   whitecapping dissipation coefficients C_{DS} and δ were altered from their default values to become $C_{DS}=1.33$ (2.1 default) and

227   $\delta = 0.5$ (default value was 0.6). Finally, a limitation to the high-frequency part of the wave spectrum corresponding to the

228   Cy43r1 ECMWF wave forecasting system (ECMWF, 2016) was also implemented and tested in order to reduce the wave

229   steepness at very high wind speeds.

230

231   **2.2.2. Model initialization, external forcing and boundary conditions**

232   The WAV component is forced with 10 m above sea surface analysis and forecast ECMWF winds at 1/8° dissemination

233   resolution. The temporal resolution is 6 h for the analysis, 3 h for the first 3 days of the forecast and 6 h for the rest of the

234   forecast cycle. From year 2021, a higher spatial (1/10° for both analysis and forecast) and temporal (hourly for forecast days

235   1-3, 3-hourly for days 4-6 and 6-hourly for days 7-10) resolution dataset is used to force the WAV component. The wind is

236   bi-linearly interpolated onto the model grids. Sea ice coverage fields used by the North Atlantic wave model are also obtained

237   from ECMWF. With respect to currents forcing, the WAV model is forced by daily averaged surface currents obtained from

238   Copernicus Marine Service Med MFC at 1/24° resolution and the North Atlantic model is forced by daily averaged surface

239   currents obtained from the Copernicus global physical model at 1/12° resolution. The WAV component runs one cycle per day

240   operating in analysis (for 24 hours in the past - previous day) and forecast (for 10 days in the future) modes. During the analysis

241   phase, model background is blended through data assimilation with available SWH satellite observations at 3-hourly intervals

242   and forced with ECMWF analyses 6-hourly winds and daily averaged surface currents.

243   The Mediterranean Sea model receives a full wave spectrum at 5-min intervals at its Atlantic Ocean open boundary from the

244   WAM implementation in the North Atlantic. The latter model is considered to have all its four boundaries closed assuming no

245   wave energy propagation from the adjacent seas. This assumption is readily justified for the north and west boundaries of the

246   North Atlantic model considering the adjacent topography which restricts the development and propagation of swell into the

247   model domain.

248

249   **2.2.3 The wave data assimilation component**

250   The assimilation module of the WAV component is based on the data assimilation scheme of WAM Cycle 4.6.2 which consists

251   of an Optimal Interpolation (OI) of the along-track Significant Wave Height (SWH) observations retrieved by altimetry and

252   then re-adjusting the wave spectrum at each grid point accordingly. This assimilation approach was initially developed by

253   Lionello et al. (1992) and consists of two steps. First, a best guess (analysed) field of significant wave height is determined by

254   OI with appropriate assumptions regarding the error covariance matrix. One of the key issues is the specification of the

255   background error covariance matrix, for the waves called P, and the observation error covariance matrix, R. The first is defined

256   as in the following Eq. (2):

257 $$P = \exp\left(\frac{d_{ij}}{l_c}\right),\qquad(2)$$

258 while the second is Eq. (3):

260 $$R = \frac{\sigma_o^2}{\sigma_b^2},\qquad(3)$$

262 where i and j are the model grid points in the longitudinal and latitudinal directions respectively, d is the distance of the
263 observation location to the grid point, l_c is the field correlation length, while σ_o^2 and σ_b^2 stand for the observation and model
264 errors, respectively. In the above expressions the error is considered as being homogeneous and isotropic. We use R=1 and the
265 correlation length l_c equal to 3 deg (~300 km).

266 Finally, the weights assigned to the observations are the elements of the gain matrix K as presented in Eq. (4):

268 $$K = PH^T[HPH^T + R]^{-1},\qquad(4)$$

270 where H is the observation operator that projects the model solution to the observation location. For the current version of
271 Med-waves, the OI analysis procedure is applied only to altimeter along-track SWH measurements although wind at 10 m
272 measurements can be assimilated as well. Prior to OI procedure, quality checked SWH observations which are available in a
273 ±1.5 hours time window are collocated with the closest model grid point and averaged.

274 During the second step, the analysed significant wave height field is used to retrieve the full dimensional wave spectrum from
275 a first-guess spectrum provided by the model itself, introducing additional assumptions to transform the information of a single
276 wave height spectrum into separate corrections for the wind sea and swell components of the spectrum. Two-dimensional wave
277 spectra are regarded either as wind sea spectra, if the wind sea energy is larger than 3/4 times the total energy, or, if this
278 condition is not satisfied, as swell. If the first-guess spectrum is mainly wind-sea, the spectrum is updated using empirical
279 energy growth curves from the model. In case of swell, the spectrum is updated assuming the average wave steepness provided
280 by the first-guess spectrum is correct, but the wind is not updated.

281 Prior to assimilation, all altimeter SWH observations are subject to a quality control procedure. Every day the system is
282 scheduled to simulate 264 hours: 24 hours in the past (analysis) blending through data assimilation model results with all
283 satellite SWH observations available followed by 240 hours forecast. The assimilation step adopted for the current version of
284 the Med-waves system equals to 3 hours.

285 **2.3 Mediterranean biogeochemical component**

286 **2.3.1. Numerical model description**
287 The BIO component consists of the Biogeochemical Flux Model (BFM, Vichi et al., 2007) coupled with the transport
288 (OGSTM) module (Salon et al., 2019). Advection, vertical and horizontal diffusion and the sinking term for the
289 biogeochemical tracers (Foujols et al., 2000) are solved by the OGSTM module that uses daily 3D velocity, diffusivities and

290 2D atmospheric fields provided by the PHY component through the offline coupling scheme (Figure 1). A source splitting
291 numerical time integration is used to couple advection and diffusion to the biochemical tracer rates.
292 BFM describes the biogeochemical cycles of carbon, nitrogen, phosphorus, silicon and oxygen through the dissolved inorganic
293 and the particulate living and non-living organic compartments (Lazzari et al., 2012; Lazzari et al., 2016). The model includes
294 four phytoplankton functional groups (i.e., diatoms, flagellates, picophytoplankton and dinoflagellates), four zooplankton
295 groups (i.e., carnivorous, and omnivorous mesozooplankton, heterotrophic nanoflagellates and microzooplankton) and
296 heterotrophic bacteria. Among the nutrients, dissolved inorganic nitrogen is simulated in terms of nitrate and ammonia. The
297 non-living dissolved organic compartment includes labile, semi-labile and refractory organic matter. A carbonate system
298 component (Cossarini et al., 2015) includes alkalinity (ALK), dissolved inorganic carbon (DIC) and particulate inorganic
299 carbon (PIC) as prognostics variables, computes CO_2 air-sea gas exchange according to Wanninkhof (2014) and provides
300 diagnostics variables such as pH, CO_2 concentration and calcite saturation horizon.
301
302 **2.3.2. Model initialization, external forcing and boundary conditions**
303 Initial condition of nutrients (nitrate, ammonia, silicate and phosphate), oxygen and carbonate variables (DIC and alkalinity)
304 consist of 16 climatological profiles homogeneously applied in each of the sub-regions represented in Figure 3. Climatological
305 profiles are computed from the EMODnet dataset (Buga et at., 2018). The other biogeochemical state variables (phytoplankton,
306 zooplankton and bacteria biomasses) are initialised in the photic layer (0–200 m) according to the standard BFM values. A 5-
307 year hindcast is run using the first year (i.e. 2017) in perpetual mode. The model has two open lateral conditions: in the Atlantic
308 Ocean and in the Dardanelles Strait. Nutrients, oxygen, DIC and alkalinity in the Atlantic (i.e., boundary at lon=9°W) are
309 provided through seasonally varying climatological profiles derived from Word Ocean Atlas (WOA 2018) and literature
310 (Alvarez et al., 2014) and a Newtonian dumping is applied. The Newtonian dumping is set between the longitudes 9°W and
311 6.5°W with a time scale relaxation term linearly varying from 1/24 1/d at 9°W to 90 1/d at 6.5°W. A Dirichlet-type scheme
312 with constant concentration values of nutrients, DIC and alkalinity derived from literature (Yalcin et al., 2017; Tugrul et al.,
313 2002; Souvermezoglou et al., 2014; Copin-Montegut, 1993; Schneider et al., 2007; Krasakopoulou et al., 2017) is applied at
314 the Dardanelles Strait. The concentrations are also tuned to provide input fluxes from Black Sea to the Mediterranean Sea
315 consistent with published estimates (Deliverable of Perseus, 2020; Yalcin et al., 2017; Tugrul et al., 2002; Copin-Montegut,
316 1993). A radiative condition is set for the other BFM tracers.
317 Terrestrial inputs include 39 rivers consistently with the PHY component. Annual nutrients input are about 46500 10^6 molN/y
318 and 881 10^6 molP/y (Salon et al., 2019). Carbon and alkalinity inputs are 9300×10^9 gC/y and 800×10^9 mol/y, respectively.
319 Estimates are derived considering typical concentrations per freshwater mass in macro coastal areas of the Mediterranean Sea
320 (Copin-Montegut, 1993; Meybech and Ragu, 1995; Kempe et al., 1991) and the river water discharges from the PERSEUS
321 dataset (Deliverable of Perseus, 2012 as before). Annual atmospheric nutrient depositions are 81300×10^6 molN/y and 1194×10^6
322 molP/y for nitrogen and phosphorus, respectively (Ribera d'Alcalà et al., 2003). Spatially constant values of atmospheric pCO2

323   are derived from the 1992-2018 time series of the ENEA Lampedusa station (Trisolino et al., 2021) with the 2019 and 2020

324   values extrapolated by linear trend.

2.3.3 The biogeochemical data assimilation component

326   The BIO component features a variational data assimilation scheme (3DVarBio) which is based on the minimization of the

327   cost function (Eq. 1) (Teruzzi et al., 2014). Minimization is computed iteratively in a reduced space using an efficient parallel

328   PETSc/TAO solver (Teruzzi et al., 2019) and the background error covariance matrix, B, is factored as $B = VV^T$, where V is a

329   sequence of linear operators: $V = V_B V_H V_V$. The horizontal error covariance operator (V_H) is a gaussian filter and includes non-

330   uniform and direction-dependent length scale correlation radius to account for anisotropic coastal assimilation (Terruzzi et al.,

331   2018) and vertical profile assimilation (Cossarini et al., 2019). The vertical error covariance operator (V_V) is based on a set of

332   0-200 m200m vertical error profiles obtained using an empirical orthogonal functions (EOFs) decomposition of a 20-yearlong

333   pre-existing biogeochemical simulation. EOFs are computed monthly for the 16 subregions with the actual vertical resolution

334   and rescaled at each grid-point considering the ratio between observation and model variances (Teruzzi et al., 2018). The

335   biogeochemical error covariance operator (V_B) is designed to preserve the ratios among phytoplankton functional types and

336   their internal carbon to nutrient quotas (Teruzzi et al., 2014) and supports monthly and spatial varying covariances between

337   dissolved inorganic nutrients (Teruzzi et al., 2021). In the most recent BIO model configuration (Teruzzi et al., 2021; Cossarini

338   et al., 2019), the assimilated biogeochemical observations are satellite multi-sensor (MODIS, VIIRS and OLCI) surface

339   chlorophyll data (Volpe et al., 2019) and quality-controlled BGC-Argo nitrate and chlorophyll profiles (Schmechtig et al.,

340   2018; Johnson et al., 2018). Ocean colour data are interpolated from original 1km resolution to the 1/24° model resolution.

341

2.4 Systems evolutions

343   The Mediterranean has been the site of major forecasting research activities since the late nineties (Pinardi and Woods, 2001;

344   Pinardi et al., 2003; Pinardi and Coppini, 2010). Before 2008, only the PHY and BIO components were present. The PHY

345   component was based on the Ocean Parallelise (OPA) code (Madec et al., 1998) with the highest available horizontal and

346   vertical resolution of 1/16° degrees (approx. 6.5 km) in horizontal and 72 vertical levels, with closed lateral boundaries, only

347   7 major rivers and implementing a weekly 3D-VAR assimilation scheme (Dobricic et al., 2007) assimilating temperature and

348   salinity vertical profiles, Sea Level Anomaly (SLA) along with track altimeter data, moreover a non-solar heat flux correction

349   was imposed through a nudging along the whole day with Sea Surface Temperature (SST) satellite gridded data.

350   A major upgrade of the PHY component was achieved in 2009 by implementing a version of the numerical model NEMOv3.1

351   including LOBC in the Atlantic Ocean (Oddo et al., 2009) and moving to a daily assimilation cycle. The first exchanges with

352   a wave model were implemented in 2010 when the PHY component was coupled hourly with WAM receiving the surface drag

353   coefficient to better represent the wind stress. In 2013 the whole operational modelling system was updated by implementing

354   an upgraded 2-way on-line coupled system based on NEMOv3.4 and WW3 (Clementi et al., 2017a) allowing for a more

355   consistent exchange between the two models. The following year the PHY general circulation module was improved by

356   accounting for the effect of atmospheric pressure effect (in addition to wind and buoyancy fluxes) and an explicit linear free

357   surface formulation using a time splitting scheme (Oddo et al., 2014), while the assimilation scheme was enhanced thanks to

358   the assimilation of Tailored Altimetry Products for Assimilation Systems (TAPAS) SLA data allowing for the application of

359   specific corrections of the altimetric original signal (Dobricic et al., 2012).

360   The PHY component delivered in 2015 included the nesting in the Atlantic Ocean through daily analysis and forecast fields

361   from the global system, while one year later the assimilation scheme was enhanced including the computation of monthly and

362   grid point EOFs and vertical observational errors varying with depth.

363   Another major PHY component evolution was achieved in 2017 when the resolution of the operational system was increased

364   to 1/24° degrees (approx. 4 km) horizontal and 141 vertical levels using the z-star vertical coordinate system, a non-linear free

365   surface formulation and the NEMOv3.6 version and 39 rivers were introduced. From year 2019 the Dardanelles Strait inflow

366   was set as a lateral open boundary condition (instead as a river runoff climatological input) allowing for a daily update of the

367   fluxes, and an improved nudging with the satellite sea surface temperature was included by correcting the heat fluxes only

368   close to midnight.

369   The WAV component was developed and released for the first time in 2017 based on WAM Cycle 4.5.4 providing on a daily

370   basis 5 days wave forecasts and simulations for the Mediterranean Sea at 1/24° horizontal resolution (Ravdas et al., 2018)

371   nested within a North Atlantic model at 1/6° resolution and forced with ECMWF 10 m winds and PHY component surface

372   currents. In March 2018 the system was upgraded by incorporating the data assimilation component to utilise available track

373   SWH satellite observations from Sentinel-3A and Jason-3. In 2019, the wave model was upgraded to Cycle 4.6.2 and the

374   duration of the forecasts were extended to 10 days. Additionally, a limitation to the high frequency part of the wave spectrum

375   was applied while modifications from default values were introduced in the input source and dissipation functions: ZALP was

376   set to 0.011 and C_{DS} and δ became 1.33 and 0.5 respectively.

377   In 2009, the first pre-operational version of the BIO component featured early versions of OGSTM transport model and BFM

378   model (Lazzari et al., 2010). The spatial resolution was 1/8°, which required a subsampling of the PHY component fields from

379   the 1/16° resolution. The Atlantic boundary was closed with a nudging term for nutrients and the land nutrients input included

380   the three major Mediterranean rivers (i.e., Po, Rhone and Nile) and the Dardanelles was treated as a river. BFM used constant

381   daily averaged irradiance to force photosynthesis (Lazzari et al., 2010).

382   Horizontal resolution aligned with the physical model in 2013 and was refined to 1/24° in 2017. Full alignment between the

383   PHY and BIO components in terms of same horizontal and vertical resolutions, bathymetry, boundaries (number and position

384   of rivers) was introduced in 2018 and remained a standard that mitigates possible approximation errors related to the use of

385   daily output of the eddy-resolving ocean general circulation model to force the transport of tracers (Salon et al., 2019).

386   Additionally, nutrient and carbon land input from 39 rivers were introduced in 2017, open boundary conditions at Dardanelles

387   Strait in 2019 and in the Atlantic Ocean in 2020 (Salon et al., 2019).

388 Since 2008, three major improvements of the BFM model have been integrated (i) the addition of the carbonate system to
389 predict alkalinity, ocean acidity and CO2 air-sea exchanges in 2016 (Cossarini et al., 2015), (ii) the revision of nutrient
390 formulation of phytoplankton in 2018 (Lazzari et al., 2016) and, (iii) in 2020, the introduction of the day-night cycle in light-
391 dependent formulation of phytoplankton (Salon et al., 2019) and of the novel light extinction coefficient (Terzic et al., 2021).
392 A major system evolution and quality improvement was achieved in 2013 with the inclusion of the assimilation of satellite
393 chlorophyll through a variational scheme with prescribed background error covariance (Teruzzi et al., 2014). Assimilation
394 method was improved in 2018 to include coastal component (i.e., non-uniform and direction-dependent horizontal covariance;
395 Teruzzi et al., 2018) and in 2019 to integrate new observations (i.e., BGC-Argo float profiles) including new parameterization
396 for the vertical and biogeochemical background error covariance (Cossarini et al., 2019).

397 In terms of operational product delivery, the BIO component has produced daily 10-day forecasts and weekly 7-day analysis
398 since 2020, fully aligned with the PHY component (Salon et al., 2019). Before that, the system produced 7-day analysis and a
399 7-day forecast once per week since 2013, while a second cycle of 7-day forecasts was added each week in 2015.

400 **3. Quality assessment**

401 The evaluation of the quality of the Med-MFC is given here only for the analysis products, leaving the assessment of the
402 forecast skill for future work. One overarching driver for the Med-MFC evolution is the continuous improvement of the
403 numerical model and data assimilation modules with respect to a well-defined set of goodness indices established for all the
404 European regional Seas (Hernandez et al., 2009). Ocean model uncertainties emerge from sources of errors relevant to the
405 ocean state, including physics, biogeochemistry, and sea ice, as well as errors in the initial state and boundary conditions (i.e.
406 atmospheric forcing and lateral open boundary conditions). Model uncertainties in ocean physics have a significant impact in
407 all other system components as, for example, in biogeochemistry and sea ice (Alvarez Fanjul et al., 2022). Our results describe
408 the quality of the Med-MFC products presenting the statistics and accuracy numbers based on a reference simulation produced
409 to calibrate and validate the operational forecasting systems, whereas the analysis of model uncertainty sources is outlined in
410 the discussion part also referring to previous specific publications.

411 **3.1. PHY component skill**

412 The skill of the physical component is assessed over a 3-year period from 2018 to 2020 (Clementi et al., 2019). The evaluation
413 is done by means of Estimated Accuracy Numbers (EANs) which consist of the root mean square differences (RMSD) and
414 bias (model minus observations) of daily mean of model outputs against satellite and in-situ observations. EANs are evaluated
415 using daily mean of model estimates interpolated on the available observations in that day: this goodness score is somewhat
416 approximated especially at the surface where daily variability is large, but this is a score used by many forecasting systems
417 (Ciliberti et al., 2022; Toledano et al., 2022; Sotillo et al., 2021; Najy et al., 2020) and we will show it for reference purposes.
418 We also use misfits, which are the difference between the model solutions and the observations at the observational time during

419   the forward model integration, for this assessment. The misfits provide quasi-independent and more accurate skill assessment

420   since they are calculated before the variational analysis and at the observational time.

421   Table 2 summarises the EAN of 3D model temperature and salinity daily mean values compared to in-situ observations, in

422   particular Argo floats and CTD profiles averaged over the three reference years. Model temperature shows small positive and

423   negative biases depending on the depth, with the largest error (maximum value of the period is 0.85°C) in the sub-surface

424   layers between 10 and 60 m, decreasing with depth. Salinity is characterised by an almost general negative small bias, meaning

425   generally lower salinities than measured, along the whole water column except for the first layer. The salinity RMSD mean

426   value is generally lower than 0.2 PSU, the error is larger in the first layers and decreases significantly below 150 m. The

427   comparison with other Copernicus Marine Service forecasting systems EAN values presented in the Quality Information

428   Document (QUID), considering that the validation periods are different, shows that the Mediterranean temperature and salinity

429   quality in terms of RMSD are aligned with all the other Copernicus forecasting systems. In particular the sea surface

430   temperature averaged RMSD with respect to satellite data ranges from 0.48°C in the North West Shelf (derived from the QUID

431   of the product NORTHWESTSHELF_ANALYSIS_FORECAST_PHY_004_013 https://doi.org/10.48670/moi-00054) to

432   0.8°C in the Baltic Sea (derived from the QUID of the product BALTICSEA_ANALYSISFORECAST_PHY_003_006

433   https://doi.org/10.48670/moi-00010), while the 3D mean temperature RMSD with respect to in-situ data ranges from 0.4°C in

434   the Mediterranean and North West Shelf to 0.7°C in the Black Sea (derived from the QUID of the product BLKSEA

435   ANALYSISFORECAST_PHY_007_001 https://doi.org/10.25423/cmcc/blksea_analysisforecast_phy_007_001_eas4) and the

436   salinity mean RMSD varies from 0.1 PSU in the Mediterranean and North West Shelf to 0.3 PSU in the Iberia-Biscay-Ireland

437   area (derived from the QUID of the product IBI_ANALYSISFORECAST_PHY_005_001 https://doi.org/10.48670/moi-

438   00027). The sea level anomaly skill is also aligned with the ones of other operational systems within the Copernicus Marine

439   Service when compared with satellite altimeter observations (from 2.2 cm in the Black Sea to 9 cm in the North West Shelf

440   area).

441   The other goodness index is computed as weekly mean root mean square error and bias using temperature and salinity misfits,

442   that are computed at FGAT. The misfits are more precise to account for surface errors since the observations are compared

443   with the model at the exact time of the day when observations are taken. This index is represented as a depth-time Hovmöller

444   diagram in Figure 4. The temperature error is seasonal (Figure 4a), with maximum values of ~1.8 ºC in the range of 30-60 m

445   depth corresponding to the depth of the mixed layer and the seasonal thermocline during the stratified season, from June to

446   November. The error is reduced to an average value of around 0.4 ºC during the vertically mixed season from December to

447   May. The temperature misfits (Figure 4c) indicate an overall overestimation of the temperature, except for the subsurface

448   layers, during winter and spring.

449   The salinity error (Figure 4b) is defined by two main structures: one that is constant throughout the year down to about 150 m

450   and the seasonal amplification during summer, as for the temperature errors. The maximum errors reach values of 0.35 PSU

451   in the summer period and decrease to 0.025 PSU below ~150 m. We argue that the background error, uniform throughout the

452   year, could be due to inaccurate advection of salinity in different sub-areas of the Mediterranean Sea. Moreover, the model

Commented [gc1]: We would like to propose to keep PSU unit for Ocean Salinity variable. This unit is typically used oceanographic papers. The definition of PSU is the one proposed in the UNESCO manual 2010 (IOC,SCORandIAPSO,2010:Theinternationalthermodynamicequatio nofseawater– 2010:Calculationanduseofthermodynamicproperties.Intergovernment alOceanographicCom)mission,ManualsandGuidesNo.56,UNESCO(E nglish),196pp.)

453 salinity bias is generally negative, i.e., the model salinity is lower than the observations (Figure 4d). This could be related to

454 the larger Atlantic water inflow with respect to literature (Soto-Navaro et al., 2010) at Gibraltar as reported in Table 3 and to

455 inaccurate mixing at Gibraltar due to the lack of tides.

456 Sea surface temperature (SST) and sea level anomaly (SLA) skills are evaluated comparing them with satellite observations:

457 model daily mean SST is compared to SST satellite L4 gridded data at 1/16° resolution (Buongiorno Nardelli et al., 2018)

458 while SLA is compared to along with track satellite altimeter observations (Taburet et al., 2019) in terms of model misfits.

459 Table 4 presents the RMSD and bias values computed for SST as well as SLA RMSD averaged in the Mediterranean Sea and

460 over the 16 sub-regions (see Figure 3). Considering SST, the RMSD values range between 0.47 °C and 0.69 °C (mean

461 Mediterranean Sea error is 0.54 °C) and the bias is generally positive, possibly caused by an overestimation of the downward

462 shortwave radiation flux which is estimated according to Reed (1977) formula, as already discussed in (Byun et al. (., 2007)

463 and Pettenuzzo et al. (2010). The SLA error ranges between 2.3 cm and 5.3 cm (mean error is 3.8 cm). The SLA skill scores

464 vary in different regions, this could be related to the spatial coverage of the observations (not homogeneous in the basin) and

465 on the limit of the 1000 m assimilation depth (due to the dynamic height operator which assumes a level-of-no-motion to

466 compute the sea level increments from temperature and salinity increments, see section 2.1.3).

467 The time variability of the model SLA accuracy is also provided by means of weekly model misfits evaluated for each available

468 satellite altimeter and averaged in the whole Mediterranean Sea as shown in Figure 5. The error ranges between 2.5 cm and

469 5.5 cm (maximum error with respect to Cryosat) with a large variability among the different satellites, with a generalised

470 increase of error during Autumn and Winter seasons.

471 **3.2. WAV component skill**

472 The quality of the wave analysis and forecast product is assessed over a three-year period from January 2018 to December

473 2020. The skill of the Mediterranean wave model is assessed by considering inter-comparisons of the model solution during

474 the 24-h analysis phase with available in-situ (SWH and mean wave period from wave buoys) and remotely sensed (SWH)

475 observations. As the latter are ingested into the model through data assimilation, the model first guess SWH (i.e. model

476 background) is used instead of model analysis.

477 Significant wave height (SWH) and mean wave period (MWP) measurements are used for data validation from 28 wave buoys

478 in the Mediterranean Sea (lower panel of Figure 7). Data quality control procedures have been applied to the in-situ

479 observations (Copernicus Marine In-Situ Team, 2020) and measurements associated with a bad quality flag are not taken into

480 consideration.

481 Figure 6 depicts scatter plots of the evaluation of the observed SWH and MWP against measurements obtained from the 28

482 buoys. For the immense number of match-up data (within the range 0 – 1.25 m), the model overestimates SWH with respect

483 to the buoy measurements (left-hand side panel). Additionally, the model underestimates SWH during more energetic events

484 (>1.25 m), except for the range 5.5-6.2 m. For large wave heights, model results underestimate SWH compared to the buoys,

485 which agrees with past findings for the Mediterranean Sea (Ardhuin et al., 2007; Korres et al., 2011). Negative SWH BIAS

486 can be attributed to errors in the forcing or inaccurate wave growth and dissipation at high wind speeds (Pineau-Guillou et al.,
487 2018). The dashed orange line (i.e. the 45° ref. line) in the Quantile-Quantile (QQ) plot stands for the unit gradient line. We
488 observe that model results follow the dashed orange line very closely, meaning the model produces well the distribution of
489 SWH observations. Although for higher waves (> 1.25 m) the model tends to underestimate SWH (except for the range 5.5-
490 6.2 m), it overproduces very large wave heights (100th, 99.97th, 99.96th, 99.95th percentiles); hence a deviation from the
491 orange dashed reference line in the QQ plot becomes prominent for very high waves. Concerning MWP, the model
492 systematically underestimates it (right-hand side panel). Despite the overall modelled MWP underestimation (BIAS = -0.314
493 s), the system tends to overestimate MWP for high percentiles/very long waves (hence we observe the deviation of the Q-Q
494 plot from the unit gradient line for very high periods). Seasonal results (not shown) for both variables SWH and MWP indicated
495 that the model adequately captures the seasonal variability. For SWH, RMSD values vary from 0.154 m in summer to 0.231
496 m in winter. Nevertheless, Scatter Index (SI) is higher in summer (0.26) than during the other seasons. Additionally, the highest
497 Pearson correlation coefficient (CORR) is observed in winter (0.963, while the lower one is equal to 0.932 and it is observed
498 in summer). The metrics reveal that the model follows better the observations in winter than during the other months since the
499 former is associated with more well-defined weather patterns and higher waves. A similar conclusion has been reached also
500 by other studies (e.g. Ardhuin et al., 2007) for the Mediterranean Sea. Summer and autumn are characterised by higher SI
501 values (0.244 and 0.260 respectively), while lower values are obtained for winter and spring (0.231 and 0.227 respectively).
502 Finally, small positive BIAS values are met for all seasons, with the highest values found in summer (0.012 m). Regarding
503 mean wave period, RMSD varies from 0.610 s in summer to 0.66 s in winter and BIAS is negative for all seasons. SI does not
504 present significant seasonal variability, with the highest value encountered in summer. Finally, CORR for MWP is higher than
505 0.8 in all seasons (values are within the range 0.859 – 0.878, while during summer CORR equals 0.792). These metrics
506 demonstrate that the model wave period (similarly to the wave height) correctly follows the observations in well-defined
507 weather conditions characterised by higher waves and longer periods, agreeing with past studies (Cavaleri and Sclavo, 2006;
508 Ravdas et al., 2018).
509 The qualification metrics for the different buoy locations in Figure 6 are plotted in Figure 7 (upper panel). RMSD at the
510 different buoy locations varies from 0.13 m to 0.31 m. SI varies from 0.17 at buoy 3732621 to 0.35 at the buoys of Malaga
511 and SARON (Aegean Sea). In general, SI values above the mean value for the whole Mediterranean Sea (0.24) are obtained
512 at wave buoys located near the coast, particularly if these are sheltered by land masses on their north-northwest (e.g. western
513 French coastline), and/or within enclosed basins characterised by a complex topography such as the Aegean Sea. As explained
514 in several studies (Ravdas et al., 2018), in these cases, the spatial resolution of the wave model is often not adequate to resolve
515 the fine bathymetric features whilst the spatial resolution of the forcing wind forcing is incapable to reproduce the fine
516 orographic effects, introducing errors to the wave analysis. The Pearson correlation coefficient (CORR) mostly follows the
517 pattern of variation of SI (in this figure we present the CORR deviation from unity). CORR ranges from 0.87 at SARON in
518 the Aegean Sea to 0.97 at the deep-water buoy 6100196 offshore Spain, which is well-exposed to the prevailing north-westerly
519 winds in the region. The BIAS varies from -0.13 m at buoy 3732621 (located north of Crete) to 0.13 m at buoy 6100021

520 located near the French coast. Its sign varies, with positive and negative values computed at almost the same number of
521 locations respectively. Figure 8 (right) shows the scatter plot between the first guess SWH and satellite observations. Here the
522 initial guess SWH refers to the model SWH before data assimilation, thus meaning semi-independent model data. In addition,
523 a scatter plot resulting from the comparison of the ECMWF forcing wind speeds (U10) and satellite measurements of U10 is
524 shown in Figure 8 (left). It is seen that ECMWF forcing overestimates U10 with respect to observations, throughout most of
525 U10 range while some underestimation is observed for high wind speeds (14 – 19 m/s). An overall ECMWF overestimation
526 of 3% is computed. On the other hand, the SWH model underestimation is about 6%. Compared to the equivalent results
527 obtained from the model-buoy comparison, a smaller scatter (by about 7%) with a larger overall bias is associated with the
528 model-satellite comparison, i.e. open ocean waves. SI values compare well at the more exposed wave buoys in the
529 Mediterranean Sea.

530 Figure 9 maps statistics of the comparison of model first-guess and satellite observations of SWH for the different sub-regions
531 of the Mediterranean Sea. The Aegean and Alboran Seas have relatively high SI values (0.21). The highest value of SI is
532 obtained for the North Adriatic Sea (0.26) followed by the South Adriatic (0.23). The lowest values (0.13-0.15) are found in
533 the Levantine Basin, the Ionian Sea, and the Southwest Mediterranean Sea. Relatively low values (0.16) are also found west
534 of the islands of Sardinia and Corsica. As discussed above, the error is due to inaccuracies associated with orographic winds
535 and/or local sea breezes and the missing representation of the complicated bathymetry in the fetch-limited, enclosed regions.
536 SWH negative bias is present in all sub-regions.

537 Finally, inter-compared to ECMWF, UK MetOffice and DMI (Danish Meteorological Institute) wave forecasting systems for
538 a different year (2014), Med-waves shows a better skill in terms of SWH with RMS errors for the Western Med buoys equal
539 to 0.227 m (0.234 m for ECMWF; 0.281 m for UK MetOffice) and 0.201 m for the central and eastern Mediterranean (0.227
540 m for ECMWF; 0.268 m for DMI).

541

3.3. BIO component skill

543 The BIO component state variables can be validated at three different uncertainty levels providing a "degree of confirmation"
544 (Oreskes et al., 1994) of different scales of variability based on the availability of reference data.

545 Near real time satellite and BGC-Argo float data provide a rigorous skill performance validation data set down to the scales of
546 the week and mesoscale dynamics for a limited set of variables: chlorophyll, nitrate and oxygen. Dataset of historical
547 oceanographic data (SOCAT dataset, Baker et al 2016); EMODnet data collection, Buga et al. (2018); Cossarini et al., (2017);
548 Lazzari et al., 2016) are used to build a reference framework of sub-regions and annual and seasonal climatological profiles to
549 validate model performance to simulate the basin wide gradients, the mean vertical profiles and the seasonal cycle. For this
550 data set it is possible to have nutrients, such as nitrate, phosphate, ammonia and silicate, as well as dissolved oxygen, dissolved
551 inorganic carbon, alkalinity and surface pCO2.

552   Lastly, a third level of validation regards those variables whose observability level is very scarce (e.g., phytoplankton biomass)
553   or based on indirect estimations (e.g., primary production, air-sea CO2 fluxes). Only confirmation of the range of variability
554   and a general uncertainty estimation can be provided for those variables (see for example the validation of model primary
555   production in von Schuckmann et al. 2020; Cossarini et al., 2020).
556   Considering the 2018-2020 reference period, the chlorophyll is very well reproduced by the BIO component, both in terms of
557   seasonal cycle and spatial gradient at surface (Figure 10) and in terms of vertical profiles at the BGC-Argo float positions
558   (Table 5). Uncertainty of surface chlorophyll is lower than 0.03 mg/m^3 with larger values registered in winter and western sub-
559   regions where the variability and the chlorophyll values are higher (Figure 10a and b). Regarding profiles, chlorophyll values
560   and vertical shapes driven by mesoscale dynamics are simulated with a high level of accuracy by the model (Salon et al., 2019;
561   Cossarini et al., 2019, 2021). Daily values of RMSD and of Pearson correlation are computed between satellite and model
562   output maps, then averaged over the two periods (Figure 10c and d). The plot of RMDS (Figure 10c) shows that higher errors
563   are registered in the western sub-regions and in winter when chlorophyll levels and variability are higher. On the other hand,
564   spatial correlation values are moderate and high in all sub-regions (i.e., values always above 0.5 except for a few sub-regions),
565   with summer values better than winter values. Considering the number of grid points in each sub-regions, all values in Figure
566   10d should be considered significantly non-zero at the 0.05 level. Indeed, Salon et al. (2019) show how, using novel metrics,
567   the BIO component reproduces with high level of accuracy not only the concentrations in the euphotic layer, but also the
568   seasonal evolution of the shape of the profiles. The depth of the deep chlorophyll maximum during summer and of the surface
569   bloom during winter, as well as the depth of the nitracline and the depth of the maximum oxygen layer, which results from the
570   interaction of physical and biogeochemical processes, are reproduced with an uncertainty of the $O(10^1)$ meters (Table 5).
571   However, the conclusions about mesoscale accuracy of the BIO component should be taken with caution since the BGC-Argo
572   observations are still relatively few in number (about 1 over 8 w.r.t. the Argo floats have biochemical sensors) and unevenly
573   spaced (e.g., southern Mediterranean Sea is less observed than northern areas).
574   As explained above, an additional verification of biogeochemical variables can be achieved for additionally 7 variables (not
575   considering chlorophyll) and two other derived variables with climatological data. An example of such comparison is shown
576   in Figure 11 for the carbonate system variables. Average maps and profiles of Alkalinity and DIC in selected sub-regions in
577   the zonal directions (coloured lines) are well superimposed to the range of variability of the historical in-situ data (grey shaded
578   areas) demonstrating the capability of the BIO component to reproduce both horizontal basin-wide gradients and vertical
579   profiles in the different areas. A slight overestimation of DIC and alkalinity (underestimation of alkalinity) is simulated in the
580   Alboran sub-region in the upper 0-100 layer.
581   As a summary of the skill performance analysis, statistics based on RMSD for all the considered model variables (Table 6)
582   reports the model uncertainty in reproducing the basin-wide values and gradients for the selected layers. Generally, larger
583   errors are computed for the upper layers where the variability (both spatial and temporal) is higher. Ammonia reports high
584   errors also in subsurface layers, which is due to a possible incorrect initialization of deep layers since the lack of data in 9 out
585   of 16 sub-regions. These numbers, which respond to the request for a synthetic measurement of Copernicus Marine Service

586 product accuracy (Hernandez et al., 2018), are consolidated by in deep skill performance analysis of BFM model in reproducing
587 chlorophyll (Lazzari et al., 2012; Teruzzi et al., 2018), nutrients (Lazzari et al., 2016; Salon et al., 2019) and carbonate system
588 variables (Cossarini et al., 2015).

589 Chlorophyll from Ocean Color is the most common variable used for validation and near real time assessment of operational
590 biogeochemical models and allows for a comparison of the forecast skill performance among the Marine Copernicus systems.
591 Results of surface chlorophyll skill scores show that the quality of the first day of forecast of the BIO component is in line
592 with those of other Copernicus models[1] (Spruch et al., 2020; Vandenbulcke et al., 2022; McEwan et al., 2021; McGovern et
593 al., 2020). In particular, the two proposed accuracy indexes (i.e., one minus scatter index and one minus the root mean square
594 error normalised on variability) of the MED model equal to 34% and 47%, which are within the ranges of the other Copernicus
595 systems: 11%-38% and 13%-73% for the two skill scores, respectively (Spruch et al., 2020; Vandenbulcke et al., 2022;
596 McEwan et al., 2021; McGovern et al., 2020).

597 For other biogeochemical variables, a direct comparison of the accuracy among Copernicus models is not straightforward,
598 given the different protocols for metrics computation, the representativeness of the available observations and the large range
599 of variability of observed values of biogeochemical variables among the European seas. Nevertheless, a rough comparative
600 assessment of the quality of Marine Copernicus biogeochemical models can be provided using published estimated EANs
601 normalized by the typical values of the variables (McEwan et al., 2021; Feudale et al., 2021; Spruch et al., 2020; Melsom and
602 Yumruktepe, 2021; McGovern et al., 2020; Vandenbulcke et al., 2021) to derive a common index of relative uncertainty. As
603 for examples, relative uncertainty of oxygen of the MED system is of the order of 2% which is in line with the other Copernicus
604 systems, except for Baltic and Black Seas systems, which show slightly higher relative errors. For nutrients, nitrate and
605 phosphate uncertainties of the MED are about 50% and 35% which are similar or slightly better than most of the other
606 Copernicus marine biogeochemical systems (i.e., ranges of 30-75% and 30-50% for nitrate and phosphate, respectively).
607 Finally, the relative uncertainty of pH simulated by the MED system is less than 0.5% while other Copernicus systems report
608 relative errors of the order of 1-2%.

609 Beside the aforementioned comparison, the MED biogeochemical system exhibits some distinguishable features: the
610 continuous monitoring of the forecast skill of surface chlorophyll since the beginning of the operational biogeochemical system
611 dating back to 2010 (Salon et al., 2019), a large number of validated variables with in-situ data (i.e., up to 10 variables, Table
612 6), the thorough use of BGC-Argo observations for near real time forecast validation (Salon et al., 2019; Cossarini et al., 2021;
613 https://medeaf.ogs.it/nrt-validation, last visit August 2022).

---

[1] Product Quality Dashboard, Green Ocean section, https://pqd.mercator-ocean.fr/, accessed 15 July 2022.

3.4. ECMWF forcing skill

A calibration/validation system of the ECMWF forcing fields used by the Med-MFC operational systems has been developed using in-situ ground meteorological observations (METAR stations) and numerical model data from ECMWF (see Figure 12). Four well-established statistical indices for validating 2 m temperature, dew point temperature, air pressure and wind speed have been defined: (a) Bias, (b) RMS Error, (c) Nash-Sutcliffe Model Efficiency Coefficient, (d) Correlation Coefficient. The atmospheric forcing Cal/Val system will become publicly available, and an example of this validation is provided in figure 12 showing daily mean wind speed time series from a METAR station (blue line) and ECMWF (red line) in the area of the Gulf of Lion during the year 2019 as well as time series of main skill metrics.

4. Conclusions and Future Perspectives

In this paper, the Med-MFC components (PHY, BIO and WAV) have been described providing an overview of their technical specifications. The PHY component provides 3D currents, temperature, salinity with the BIO and WAV components daily, with daily mean values. This model system is flexible enough that improvements can be carried out separately on the three components, considering different levels of maturity of the numerical modelling parametrizations, the data assimilation components and the validation data sets. A different data assimilation system is run for each component making the best use of all available data from satellite and in-situ observations, the effort is to assimilate as much data as possible and use background or model uncertainties to account for the missing couplings. The 3 components accuracy has been evaluated for a common three-year period, from January 2018 to December 2020.

The PHY component has been validated comparing model data with respect to in-situ and satellite observations showing a good accuracy in representing the spatial pattern and the temporal variability of the temperature, salinity and sea level in the Mediterranean Sea. In particular, the model has a warm surface temperature bias of +0.12 °C when compared to satellite SST. The water column temperature error has a clear seasonal signal with the largest errors at the depth of the surface mixed layer and the seasonal thermocline. The model error in salinity is higher in the first layers and decreases significantly below 150 m. The SLA presents a mean average error of 3.8 cm on the three-year averaged period for the whole basin.

The WAV component was extensively validated for the 3-year period using all available in-situ and satellite observations in the Mediterranean Sea. All statistical values calculated and presented here showed a very good system performance. It is concluded that the Mediterranean SWH is accurately simulated by the WAV component. The typical SWH difference with observations (RMSE) over the whole basin is 0.21 m (0.197 m for in-situ and 0.228 m for satellite observations) with a bias ranging from -0.137 m to -0.005 m, when the comparison is against the in-situ observations, and from to -0.088 m to 0.131 m when the comparison is with satellites. The scatter index (SI) exhibits low values (0.13-0.17) over the majority of the basin and relatively higher values (0.18-0.21) over the Aegean, Alboran, Ligurian and East Levantine Sea, with the highest SI value encountered in the North Adriatic Sea (0.26). As explained, the occurrence of higher SI values is mainly related to the quality

645 of ECMWF winds in fetch-limited areas of the basin where the orographic effects play an important role and the difficulties
646 of wave models to appropriately resolve complicated bathymetry and coastline.

647 Overall, the quality of the WAV component stems from the ECMWF wind forcing that drives the wave dynamics, data
648 assimilation, forcing from Med-PHY surface currents and improved parameterization of wave wind source and dissipation
649 terms of WAM model. In particular, the WAV component assimilates satellite altimetry data with a well calibrated stand-alone
650 OI scheme and implements regular updates and improved parameterization independently from the other components. Given
651 that wind forcing quality has a substantial influence on the model response, a considerable part of the wave product uncertainty,
652 especially under high winds or extreme conditions, is related to the wind forcing uncertainty and can be substantially improved
653 by undertaking the ensemble approach in wave forecasting. The lower accuracy of the wave product in semi-enclosed regions
654 of the Mediterranean Sea (e.g. Adriatic and Aegean Seas) can be related to the current spatiotemporal resolution of the wind
655 forcing. Near the coast, unresolved topography by the wind and wave models and fetch limitations causes the wave model
656 performance to deteriorate. In particular, the WAV component assimilates satellite altimetry data with a well calibrated stand-
657 alone OI scheme and implements regular updates and improved parameterization independently from the other components.
658 Given that wind forcing quality has a substantial influence on the model response, a considerable part of the wave product
659 uncertainty, especially under high winds or extreme conditions, is related to the wind forcing uncertainty and can be
660 substantially improved by undertaking the ensemble approach in wave forecasting. The lower accuracy of the wave product
661 in semi-enclosed regions of the Mediterranean Sea (e.g. Adriatic and Aegean Seas) can be related to the current spatiotemporal
662 resolution of the wind forcing. Near the coast, unresolved topography by the wind and wave models and fetch limitations cause
663 the wave model performance to deteriorate.

664 The BIO system has defined a validation framework (Salon et al., 2019) based on multivariate (e.g., more than 10 variables)
665 and multilevel metrics that include GODAE class 1 and class 4 statistics and process- oriented metrics. Particularly interesting,
666 the present validation framework includes also near real time observations (i.e. satellite and BGC-Argo) that shows average
667 errors in the 0-200 m layer of 0.04 mg/m^3, 0.4 mmol/m^3 and 16.8 mmol/m^3 for chlorophyll, nitrate and oxygen, respectively.
668 Thus, the validation framework represents a robust benchmark for the future improvements of the Mediterranean BIO model.
669 Indeed, as detailed in Salon et al. (2019) and Cossarini et al. (2021), critical sources of the BIO model errors include unresolved
670 Atlantic boundary conditions as well as land-sea and atmospheric-sea forcing uncertainty in model parameterization and
671 inconsistency of coupled physical-biogeochemical processes.

672 The value and reliability of the Med-MFC systems is demonstrated by the several downscaling coastal model systems and
673 downstream applications that use its outputs operationally. The CYCOFOS – Cyprus Coastal Ocean Forecasting and Observing
674 System (Zodiatis et al., 2003), which is a sub-regional forecasting and observing system in the Eastern Mediterranean
675 Levantine Basin, uses the Med-MFC output to set its boundary conditions. The Med-MFC outputs are used as initial and lateral
676 boundary conditions by the physical and wave ocean system MITO, which provides 5-day forecasts at resolution up to 1/48°
677 (Napolitano et al., 2022). The Southern Adriatic Northern Ionian coastal Forecasting System (SANIFS), which is a coastal-
678 ocean operational system providing short-term forecasts since September 2014 (Federico et al., 2017). It is built on the

679 unstructured-grid finite-element three-dimensional hydrodynamic SHYFEM model and is based on a downscaling approach

680 starting from the large-scale system Med-MFC which provides the open-sea fields.

681 The CADEAU physical-biogeochemical forecast system of the Northern Adriatic Sea (Bruschi et al., 2021) is based on a high

682 resolution (up to 700m) application of the MITgcm-BFM model (Cossarini et al., 2017) targeting water quality and

683 eutrophication and uses the daily Med-MFC products for initialization and to constrain the southern boundary.

684 In addition, the GUTTA-VISIR system, which can be defined as a tactical, global-optimization, single-objective, deterministic

685 model system for ship route planning (Mannarini et al., 2015 and 2016; Mannarini and Carelli, 2019), uses the analysis and

686 forecast wave and current fields from the Med-MFC in conjunction with wind fields from ECMWF.

687 Since 2008 the Med-MFC components have been continuously upgraded and substantially improved. The system evolution

688 will continue also in the future following the main drivers of the three components: the Copernicus Marine Service users.

689 Considering the PHY system, the users need finer spatial scales and higher time frequencies of the products especially for

690 improving the representation of the coastal scale and limited area processes in nested models, thus providing a unique

691 opportunity to model the coastal areas at the resolution of few hundred meters using nesting schemes as demonstrated in

692 Federico et al. (2017) and Trotta et al. (2021) and others. Users also require higher accuracy in storm surge forecasting, which

693 can be achieved by including the explicit representation of the tidal forcing to resolve non-linear interactions between

694 astronomical and internal tides with the baroclinic circulation. An upgrade of lateral open boundary conditions in the Atlantic

695 and the Black Sea would provide better evaluation of the transport at Gibraltar, and improved dynamics in the north Aegean

696 Sea. Higher frequency river runoff data from hydrological models, as well as more accurate salinity values at river mouths,

697 would provide better salinity skill not only along the coastal areas but in the whole basin. Another important goal for the future

698 is to assimilate Argo and drifter trajectories (Nelson et al., 2016) and gliders (Dobricic et al., 2009) data as well as sea level

699 anomaly in coastal areas. Finally, future efforts should consider ensemble forecasting to recast the deterministic forecast within

700 a probabilistic framework assessing the modelling uncertainties (Pinardi et al., 2011; Millif et al., 2009; Thoppil et al., 2021;

701 Barton et al., 2021).

702 User needs for the future evolution of the WAV component indicate the increase of the frequency of the wave analyses, making

703 available larger data sets such as the wave spectra and dedicated products (like the directional spread at peak frequency and

704 different parts of the wave spectrum). The required increased accuracy in wave height and mean periods predictions can be

705 mainly achieved by improving the quality of the wind forcing which is the main driving force of wave models. Bias correction

706 of ECMWF winds and further downscaling of ECMWF forecasts is expected to improve winds and consequently wave product

707 quality especially in semi-enclosed areas (e.g. Adriatic, Aegean) and near the coast. Assimilation upgrades with the ingestion

708 of multi-mission significant wave heights at 5Hz and in-situ wave heights measurements from HF Radars will improve

709 accuracy in coastal areas of the Mediterranean Sea while the inclusion of spectral information in the near future (e.g. CFOSAT

710 wave spectrum) will further improve the prediction of the sea state. Finally the development of a WAV ensemble prediction

711 based on ECMWF operational ensemble winds is expected to improve the existing accuracy of the deterministic forecast at

712 lead times beyond 48 hours providing in parallel uncertainty estimates of wave parameters.

713 User requirements for the BIO component developments include improved quality and products tailored for ecosystem and
714 coastal applications. The validation results have contributed to identify ameliorable model process representations and model
715 parameter estimates that can be improved. These include better representation of vertical nutrient and plankton dynamics, a
716 greater number of phytoplankton functional types and zooplankton compartments to describe the diversity of the plankton
717 community and the different energy and matter pathways in the ecosystem. In addition, the integration of optics and
718 biogeochemistry, including novel hyperspectral and high-resolution radiometric data, can be used to better represent
719 photosynthesis and light-related processes and to calibrate parameters of important ecosystem processes (Lazzari et al., 2021).
720 Assimilation of new in-situ profile sensors and variables (e.g., BGC-Argo Float and Glider) will help increase the reliability
721 of BIO products, especially along the water column (Cossarini et al., 2019). Higher quality vertical dynamics can be achieved
722 through better representation of vertical model error covariances by ensemble (Carrassi et al., 2018) or joint physical-
723 biogeochemical data assimilation techniques. Finally, revising nutrient and carbon inputs from rivers (e.g., from monthly
724 climatologies to daily observations or model predictions) will allow better resolution of coastal dynamics and coastal-offshore
725 patterns in critical areas.

726 A companion manuscript (Part II), in preparation, will demonstrate the capacities of the Med-MFC components in describing
727 the Medicane effects on the ocean. In particular, the Med-MFC physics, biogeochemistry and waves components will be used
728 to describe the effects of Medicane Zorbas (27-30 September 2018) on the ocean variables.

729
730
731

732 **Author Contributions:** G.C. (Coppini) and E.C. coordinated the preparation of the paper in collaboration with G.C. (Cossarini) and G.K.

733 E.C., G.C. (Cossarini) G.K., P.L., A.T., G.B., J.P, A.C.G., A.A., R.E., A.C., D.D., S.M., A.N., N.P., M.R. contributed to the system and
734 models development; V.L., A.G., L.F., C.A., V.D., A.M., A.C.G, A.Z., C.O., E.C. contributed to the model validation and assessment; R.L.,
735 M.D., A.M., A.B., GL.C., contributed to the operational activities. All authors contributed to the final version of the paper.

736 **Funding:** This work has been funded through the EU Copernicus Marine Med-MFC Service Contact n.74.

737 **Acknowledgments:** This study has been conducted using EU Copernicus Marine Service Information. Within the Copernicus Marine
738 Service of the Med-MFC, CMCC is in charge of the coordination of the service and responsible for the Physics (ocean circulation) Production
739 Unit, OGS is responsible for the BIO (biogeochemical) Production Unit and HCMR is responsible for the Wave Production Unit. The authors
740 thank CINECA (Italian supercomputer centre) for the technical support provided in the biogeochemical component production workflow.
741 The Authors thank Dr. George Zodiatis and Orion team for the collaboration on the development of the atmospheric forcing validation tool.
742 The authors thank the anonymous reviewers for their valuable revisions.

743 **Conflicts of Interest:** The authors declare no conflict of interest

744

745

Appendix A

746

747

748   Table A1. List of the NEMO and WW3 numerical setup for the PHY component.

749

Parameter	Value
NEMO model version	3.6
Horiz. Resolution	1/24º
Vertical discretization	141 z levels with partial cells
Vertical coordinates	Z-star
Time-step	240 s
Number of barotropic iterations	100
Free-surface formulation	Non-Linear free surface with split-explicit free surface
Air-sea fluxes	MFS-Bulk formulae
Atmospheric Pressure	Yes
Wave coupling	Neutral drag coefficient
Runoff	Surface boundary condition with specific treatment at river mouth and prescribed river salinity
Sea Surface Restoring T/S	only for temperature
Solar radiation penetration	2-band exponential penetration (insert the decay length and the transmission coeff)
Lateral momentum B.C.	No-slip
Lateral Open B.C.	Flather open boundary condition for barotropic currents, Orlansky for total currents and tracers
Bottom B.C	Non-linear friction with logarithmic formulation
Equation of State	EOS-80
Tracer Advection	Up-stream/MUSCL

Tracers Horiz. Diffusivity	Bi-Laplacian coeff = -1.2.e8 [m4/s]
Momentum Horiz. Viscosity	Bi-Laplacian coeff = -2e.8 [m4/s]
Momentum Advection	Vector form (energy and enstrophy cons. scheme)
Turbulent vertical viscosity scheme	Richardson number dependent formulation following Pacanowsky Philander (1981) and Lermousiaux (2001) adjustment
Background Vertical Visc.	1.2e-6 [m2/s]
Background Vertical Diff.	1.0e-7 [m2/s]
Vertical time stepping scheme	Implicit
WW3 model version	3.14
Horiz. Resolution	1/24°
Number of frequencies	30
Number of directions	24
Time-step (global)	240 s
Wind input term	Janssen's quasi-linear theory (Jansen, 1989; Jansen, 1991)
Wave dissipation term	Hasselmann (1974) according to Komen et al. (1984)
Non-linear wave-wave interaction term	Discrete Interaction Approximation (DIA, Hasselmann et al., 1985)
Coupling with NEMO	Sea surface currents, sea surface temperature

750

751

752   **Table A2.** List of the WAM model set up for the WAV component.

Parameter	Value
WAM model version	Cycle 4.6.2
Horiz. Resolution	1/24°

Geographical domain	18.125°W - 36.2917°E 30.1875°N - 45.9792°N.
Depth map	GEBCO 30arc-second
Number of frequencies	32
Number of directions	24
Time-step (propagation)	60 s
Time-step (sources)	360 s
Deep/Shallow mode	Shallow
10 m winds	ECMWF 10 m analyses and forecast winds
C_{DS}, δ	1.33, 0.5
ZALP	0.011
Surface currents coupling	Offline coupled with Med-MFC NRT daily surface currents
Data assimilation	Optimal Interpolation method / Altimeter satellite data provided by Copernicus Marine Service are assimilated in the wave model.

753
754

755

756   **Table A3.** List of the OGSTM-BFM model set up for the BIO component.

Parameter	Value
OGSTM model version	4.1
BFM model version	5.0
3DVarBio version	3.3
Horiz. Resolution	1/24o
Geographical domain	9.0°W - 36.2917°E 30.1875°N - 45.9792°N.
OGSTM: physical forcing	U, V, W, eddy diffusivity, SSH
OGSTM: timestep	450 s
OGSTM: off-line coupling frequency	1 d
OGSTM: advection scheme	Smolarkiewicz
OGSTM: horizontal diffusion	Bi-Laplacian coefficient -3.e9 [m4/s]
OGSTM: vertical diffusion scheme	implicit 2nd order
BFM parameters for Phytoplankton, Zooplankton, Bacteria, DOM and POM formulation	as in (Lazzari et al., 2012) and 2016
BFM light: type of model	instantaneous light from short wave radiation, light at the centre of the grid cell
BFM light: Fraction of Photosynthetically Available Radiation	0.40
BFM light: conversion W/m2 to moli quanta/m2/s	1./0.217 Watt / umol photons
BFM light: background extinction coeff.	0.0435 1/m
BFM light: specific attenuation coefficient of particulate	0.001 m2/mgC

BFM carbonate system: solver using total alkalinity and DIC	SolveSAPHE v1.0.1 routines (Munhoven, 2013)
BFM carbonate system: K0, solubility of co2 in the water (K Henry)	Weiss 1974
BFM carbonate system: k1 and k2 constants for carbonic acid	Mehrbach et al. (1973) refit, by Lueker et al. (2000) (total scale)
BFM carbonate system: Kb constant for boric acid	Millero p.669 (1995) using data from Dickson (1990) (total scale)
BFM carbonate system: k1p, k2p and k3p constants of phosphoric acid	Millero (1974)
BFM carbonate system: Ksi constant of orthosilicic acid	Millero (1995)
BFM carbonate system: Kw of water dissociation	Millero (1995)
BFM carbonate system: ks of sulfuric acid	Dickson (1990)
BFM carbonate system: kf of folic acid	Perez & Fraga (1987) recom. by Dickson et al., (2007)
BFM carbonate system: air-sea exchange model	Wannikoff et al., 2014
3DVarBio: max depth of assimilation	200 m
3DVarBio: n. of vertical EOFs	26
3DVarBio: horizontal correlation radius	variable in X and Y; average 15 km (Teruzzi et al., 2018)
3DVarBio: solver for cost function J	quasi-Newton L-BFGS minimizer
3DVarBio: Minimum gradient of J	1.0E-11
3DVarBio: Percentage of initial gradient	0.01
3DVarBio: n. of interactions of recursive filter	4

757
758

759

760

761 **Table A.4.** River sources implemented as freshwater inputs in the physical and biogeochemical models, including river name, the annual

762 mean runoff and the imposed salinity at river mouth.

763

764

River Name	Mean annual Runoff [m3/s]	Salinity at river mouth [psu]
Ebro	432	30
Rhone	1707	25
Po	1519	18
Buna-Bojana	675	15
Seman	201	15
Vjosa	183	15
Nile	475	8
Aude	59	15
Arno	88	15
Tevere	181	15
Volturno	63	15
Medjerda	59	15
Reno	67	15
Adige	232	15
Brenta	163	15
Piave	129	15
Livenza	96	15
Tagliamento	79	15
Isonzo	175	15
Lika	84	15
Krka	57	15
Neretva	239	15
Trebisnjica	93	15
Mati	99	15
Shkumbini	54	15
Arachtos	75	15
Acheloos	106	15
Pineios	67	15
Axios	97	15
Struma	81	15
Maritza	166	15
Gediz	53	15
Buyuk Menderes	106	15
Köprüçay/Eurimedonte	85	15
Manavgat	122	15
Goksu	203	15
Seyhan	200	15
Ceyhan	231	15
Orontes	94	15

765

References

Adani, M., Dobricic, S., and Pinardi N.: Quality Assessment of a 1985–2007 Mediterranean Sea Reanalysis, J. Atmos. Oceanic Technol., 28, 569–589., doi:10.1175/2010JTECHO798.1, 2011.

Alves, J.-H.G.M.: Numerical modeling of ocean swell contributions to the global wind-wave climate, Ocean Model, 11, 98–122. doi:10.1016/j.ocemod.2004.11.007, 2006.

Álvarez, M., Sanleón-Bartolomé, H., Tanhua, T., Mintrop, L., Luchetta, A., Cantoni, C., et al.: The CO_2 system in the Mediterranean Sea: a basin wide perspective, Ocean Sci. 10, 69–92. doi: 10.5194/os-10-69-2014, 2014.

Alvarez Fanjul, E., Ciliberti, S., and Bahurel, P.: Implementing Operational Ocean Monitoring and Forecasting Systems,. Paris, France, IOC-UNESCO, 376pp. & Annexes, (GOOS-275). DOI: https://doi.org/10.48670/ETOOFShttps://doi.org/10.48670/ETOOFS, 2022.

Ayoub, N., Le Traon, P.-Y., and De Mey: P. A description of the Mediterranean surface variable circulation from combined ERS-1 and Topex/Poseidon altimetric data, J. of Mar. Syst. 18 (1–3), 3–40, 1998.

Ardhuin, F., Bertotti, L., Bidlot, J. R., Cavaleri, L., Filipetto, V., Lefevre, J. M., and Wittmann, P.: Comparison of wind and wave measurements and models in the Western Mediterranean Sea, Ocean Eng., 34, 526–541, https://doi.org/10.1016/j.oceaneng.2006.02.008, 2007.

Artuso, F., Chamard, P., Piacentino, S., Sferlazzo, D. M., De Silvestri, L., Di Sarra, A., and Monteleone, F.: Influence of transport and trends in atmospheric CO_2 at Lampedusa, Atmospheric Environment, 43(19), 3044-3051, 2009.

Bakker, D. C. E., Pfeil, B., Smith, K., Hankin, S., Olsen, A., Alin, S. R., Cosca, C., et al.: An update to the Surface Ocean CO_2 Atlas (SOCAT version 2), Earth Syst. Sci. Data, 6, 69-90, doi:10.5194/essd-6-69-2014, 2014.

Barton N.,E. Metzger J., C. A. Reynolds, B. Ruston, C. Rowley, O. M. Smedstad, J. A. Ridout, A. Wallcraft, S. Frolov, P. Hogan, M. A. Janiga, J. F. Shriver, P. McLay, P. Thoppil, A. Huang, W. Crawford, T. Whitcomb, C. H. Bishop, L. Zamudio, M. Phelps: The Navy's Earth System Prediction Capability: A new global coupled atmosphere-ocean-sea ice prediction system designed for daily to subseasonal forecasting. Barton N., Metzger E. J., Reynolds, C. A., Ruston, B., Rowley, C., Smedstad, O. M., et al.: The Navy's Earth System Prediction Capability: A new global coupled atmosphere-ocean-sea ice prediction system designed for daily to subseasonal forecasting, Earth Space Sci. 8, e2020EA001199, 2021.

Bergamasco, A. and Malanotte-Rizzoli, P.: The circulation of the Mediterranean Sea: a historical review of experimental investigations, Adv. Oceanogr. Limnol, 1:1, 11-28, DOI: 10.1080/19475721.2010.491656, 2010.

Brassington, G. B.: Forecast Errors, Goodness, and Verification in Ocean Forecasting. Journal of Marine Research, Volume 75, Number 3, pp. 403-433(31). https://doi.org/10.1357/002224017821836851, 2017.

Bruschi, A., Lisi, I., De Angelis, R., Querin, S., Cossarini, G., Di Biagio, V., et al.: Indexes for the assessment of bacterial pollution in bathing waters from point sources: The northern Adriatic Sea CADEAU service, Journal of Environmental Management, 293, 112878, 2021.

Byun, D. S. and Pinardi, N.: Comparison of Marine Insolation Estimating methods in the Adriatic Sea, Ocean Sci. J. 42(4), 211–222, 2007.

812

813 Buongiorno Nardelli, B., Tronconi, C., Pisano, A., and Santoleri, R.: High and Ultra-High resolution processing of satellite
814 Sea Surface Temperature data over Southern European Seas in the framework of MyOcean project, Rem. Sens. Env., 129, 1-
815 16, doi:10.1016/j.rse.2012.10.012, 2013.
816
817 Buga, L., Sarbu, G., Fryberg, L., Magnus, W., Wesslander, K., Gatti, J., et al.: EMODnet Chemistry Eutrophication and
818 Acidity aggregated datasets v2018, https://doi.org/10.6092/EC8207EF-ED81-4EE5-BF48-E26FF16BF02E, 2018.
819
820 Canu, D., Ghermandi, A., Nunes, P., Lazzari, P., Cossarini, G., and Solidoro, C.: Estimating the value of carbon
821 sequestration ecosystem services in the Mediterranean Sea: An ecological economics approach, Global Environmental
822 Change. 32. 10.1016/j.gloenvcha.2015.02.008, 2015.
823
824 Carrassi, A., Bocquet, M., Bertino, L., and Evensen, G.: Data assimilation in the geosciences: An overview of methods, issues,
825 and perspectives, Wiley Interdisciplinary Reviews: Climate Change, 9(5), e535, 2018.
826
827 Cavaleri, L. and Sclavo, M.: The calibration of wind and wave model data in the Mediterranean Sea, Coast. Eng. 53, 613–
828 627, 2006.
829
830 Cessi, P., Pinardi, N., and Lyubartsev, V.: Energetics of Semienclosed Basins with Two-Layer Flows at the Strait, J. Phys.
831 Oceanogr., 44, 967–979. doi: 10.1175/JPO-D-13-0129.1, 2014.
832
833 Ciliberti, S.A., Jansen, E., Coppini, G., Peneva, E., Azevedo, D., Causio, S., et al.: The Black Sea Physics Analysis and
834 Forecasting System within the Framework of the Copernicus Marine Service. J. Mar. Sci. Eng., 10, 48.
835 https://doi.org/10.3390/jmse10010048, 2022.
836
837 Clementi, E., Oddo, P., Drudi, M., Pinardi, N., Korres, G., and Grandi, A.: Coupling hydrodynamic and wave models: first
838 step and sensitivity experiments in the Mediterranean Sea, Oc. Dyn., doi: https://doi.org/10.1007/s10236-017-1087-7, 2017a.
839
840 Clementi, E., Pistoia, J., Delrosso, D., Mattia, G., Fratianni, C., Storto, A., et al.: A 1/24 degree resolution Mediterranean
841 analysis and forecast modelling system for the Copernicus Marine Environment Monitoring Service, Extended abstract to the
842 8th EuroGOOS Conference, Bergen, http://eurogoos.eu/download/publications/EuroGOOS-2017-Conference-
843 Proceedings.pdf, 2017b.
844
845 Clementi, E., Pistoia, J., Escudier, R., Delrosso, D., Drudi, M., Grandi, A., et al..: Mediterranean Sea Analysis and Forecast
846 (CMEMS MED-Currents EAS5 system, 2017-2020) [Data set], Copernicus Monitoring Environment Marine Service
847 (CMEMS), https://doi.org/10.25423/CMCC/MEDSEA_ANALYSIS_FORECAST_PHY_006_013_EAS5, 2019.
848
849 Copin-Montegut, C.: Alkalinity and carbon budgets in the Mediterranean Sea. Global Biogeochemical Cycles, 7(4), pp. 915-
850 925, 1993.
851 Copernicus Marine In-Situ Team and Copernicus In Situ TAC, Real Time Quality Control for WAVES, CMEMS-INS-
852 WAVES-RTQC. https://doi.org/10.13155/46607, 2020.
853 Cossarini, G., Mariotti, L., Feudale, L., Teruzzi, A., D'Ortenzio, F., Tallandier, V., and Mignot A.: Towards operational 3D-
854 Var assimilation of chlorophyll Biogeochemical-Argo float data into a biogeochemical model of the Mediterranean Sea,
855 Ocean Model, 133, 112–128, https://doi.org/10.1016/j.ocemod.2018.11.005, 2019.
856
857 Cossarini, G., Querin, S., Solidoro, C., Sannino, G., Lazzari, P., Di Biagio, V., and Bolzon, G.: Development of
858 BFMCOUPLER (v1.0), the coupling scheme that links the MITgcm and BFM models for ocean biogeochemistry
859 simulations, Geosci. Model Dev., 10, 1423–1445, https://doi.org/10.5194/gmd-10-1423-2017, 2017.
860
861 Cossarini G., Lazzari P., and Solidoro, C.: Spatiotemporal variability of alkalinity in the Mediterranean Sea, Biogeosciences,
862 12, 1647–1658, https://doi.org/10.5194/bg-12-1647-2015, 2015.
863

864 Cossarini G., Bretagnon M., Di Biagio V., Fanton d'Andon O., Garnesson P., Mangin A., and Solidoro C.: Primary
865 production, Copernicus Marine Service Ocean State Report, Issue 3, J. Oper. Oceanogr., 12:sup1, s88–s91; DOI:
866 10.1080/1755876X.2020.1785097, 2020.
867
868 Cossarini, G., Feudale, L., Teruzzi, A., Bolzon, G., Coidessa, G., Solidoro, C., Di Biagio, V., Amadio, C., Lazzari, P.,
869 Brosich, A. and Salon, S.: High-resolution reanalysis of the Mediterranean Sea biogeochemistry (1999–2019). Frontiers in
870 Marine Science, 8, 1537, 2021.
871
872 Deliverable D4.6: SES land-based runoff and nutrient load data (1980 2000), edited by Bouwman L. and van Apeldoorn D.,
873 2012 PERSEUS H2020 grant agreement n. 287600.
874
875 Delrosso, D.: Numerical modelling and analysis of riverine influences in the Mediterranean Sea, PhD Thesis, Alma Mater
876 Studiorum Università di Bologna. DOI 10.6092/unibo/amsdottorato/9392, 2020.
877
878 Desroziers, G., Berre, L., Chapnik, B., and Poli, P.: Diagnosis of observation, background and analysis-error statistics in
879 observation space, Q.J.R. Meteorol. Soc. 131: 3385–3396. doi: 10.1256/qj.05.108, 2005.
880
881 Dobricic, S. and Pinardi, N.: An oceanographic three-dimensional variational data assimilation scheme, Ocean modelling,
882 22: 89-105 (2008), doi:10.1016/j.ocemod.2008.01.004, 2008.
883
884 Dobricic, S., Pinardi, N., Adani, M., Tonani, M., Fratianni, C., Bonazzi, A., and Fernandez, V.: Daily oceanographic
885 analyses by the Mediterranean basin scale assimilation system, Ocean Sciences, 3, 149-157, doi:10.5194/os-3-149-2007,
886 2007.
887
888 Dobricic, S., Dufau C., Oddo P., Pinardi N., Pujol I., and Rio M.-H.: Assimilation of SLA along track observations in the
889 Mediterranean with an oceanographic model forced by atmospheric pressure, Ocean Sci., 8, 787-795, doi:10.5194/os-8-787-
890 2012, 2012.
891
892 Dobricic, S., Pinardi, N., Testor, P., and Send, U.: Impact of data assimilation of glider observations in the Ionian Sea
893 (Eastern Mediterranean), Dynamics of Atmospheres and Oceans, 50, 78-92, doi:10.1016/j.dynatmoce.2010.01.001, 2010.
894
895 ECMWF IFS Documentation CY43R1, Part VII: ECMWF Wave Model, Book chapter, ECMWF, 2016.
896
897 Escudier, R., Clementi, E., Omar, M., Cipollone, A., Pistoia, J., Aydogdu, A., et al.: Mediterranean Sea Physical Reanalysis
898 (CMEMS MED-Currents) (Version 1) [Data set], Copernicus Monitoring Environment Marine Service (CMEMS),
899 https://doi.org/10.25423/CMCC/MEDSEA_MULTIYEAR_PHY_006_004_E3R1, 2020.
900
901 Escudier, R., Clementi, E., Cipollone, A., Pistoia, J., Drudi, M., Grandi, A., et al.: A High Resolution Reanalysis for the
902 Mediterranean Sea, Front. Earth Sci. 9:702285. doi: 10.3389/feart.2021.702285, 2021.
903
904 Federico, I., Pinardi, N., Coppini, G., Oddo, P., Lecci, R., and Mossa, M.: Coastal ocean forecasting with an unstructured
905 grid model in the southern Adriatic and northern Ionian seas, Nat. Hazards Earth Syst. Sci., 17, 45–59,
906 https://doi.org/10.5194/nhess-17-45-2017, 2017.
907
908 Fennel, K., Gehlen, M., Brasseur, P., Brown, C.W., Ciavatta, S., Cossarini, G., et al.: Advancing Marine Biogeochemical
909 and Ecosystem Reanalyses and Forecasts as Tools for Monitoring and Managing Ecosystem Health, Front. Mar. Sci., 6,
910 UNSP 89, doi: 10.3389/fmars.2019.00089, 2019.
911
912 Feudale, L., Bolzon, G., Lazzari, P., Salon, S., Teruzzi, A., Di Biagio, V., Coidessa, G., and Cossarini, G.: Mediterranean
913 Sea Biogeochemical Analysis and Forecast (CMEMS MED-Biogeochemistry, MedBFM3 system) (Version 1) [Data set],
914 Copernicus Monitoring Environment Marine Service (CMEMS),
915 https://doi.org/10.25423/CMCC/MEDSEA_ANALYSISFORECAST_BGC_006_014_MEDBFM3
916 2021https://doi.org/10.25423/CMCC/MEDSEA_ANALYSISFORECAST_BGC_006_014_MEDBFM3 2021.

Flather, R. ARA.: A tidal model of the north–west European continental shelf, Mem. Soc. R. Sci. Liege, 10, pp. 141–164, 1976.

Fourrier M., Coppola L., Claustre H., D'Ortenzio F., Sauzède R., and Gattuso, J-P.: A Regional Neural Network Approach to Estimate Water-Column Nutrient Concentrations and Carbonate System Variables in the Mediterranean Sea: CANYON-MED. Front. Mar. Sci. 2020, 7, 620, 2021.

Giesen, R., Clementi, E., Bajo, M., Federico, I., Stoffelen, A., and Santoleri R.: The November 2019 record high water levels in Venice, Italy. In: Copernicus Marine Service Ocean State Report, Issue 5, Journal of Operational Oceanography, 14:sup1, s140–s148; DOI: 10.1080/1755876X.2021.1946240, 2021.

Gunther, H., Hasselmann, H., and Janssen, P.A.E.M.: The WAM model cycle 4, DKRZ report n. 4, 1993.

Janssen, P.A.E.M.: Wave induced stress and the drag of air flow over sea wave, J. Phys. Ocean., 19, 745-754, 1989.

Janssen, P.A.E.M.: Quasi-Linear theory of wind wave generation applied to wave forecasting, J. Phys. Ocean., 21, 1631-1642, 1991.

Johnson, K., Pasqueron De Fommervault, O., Serr, R., D'Ortenzio, F., Schmechtig, C., Claustre, H., and Poteau A.: Processing Bio-Argo nitrate concentration at the DAC Level, Version 1.1, March 3rd, IFREMER for Argo Data Management, 22pp. DOI: http://doi.org/10.13155/46121, 2018.

Hasselmann, K., On the spectral dissipation of ocean waves due to whitecapping, Boundary-Layer Meteorol., 126, 107 – 127, 1974.

Hasselmann K., Allender J. H., and Barnett, T. P.: Computations and parameterizations of the nonlinear energy transfer in a gravity wave spectrum. Part II: Parameterizations of the nonlinear energy transfer for application in wave models, J. Phys. Oceanogr.,15, 1378–1391, 1985.

Hasselmann, K., Hasselmann, K., Barnett, T.P., Bouws, E., Carlson, H., Cartwright, D.E., et al.: Measurements of wind–wave growth and swell decay during the Joint North Sea Wave Project (JONSWAP), Dtsch. Hydrogr. Z., 8, 1–95, 1973.

Hernandez, F., Bertino, L., Brassington, G., Chassignet, E., Cummings J., Davidson F., et al.: Validation and intercomparison studies within GODAE, Oceanography 22(3): 128–143, https://doi.org/10.5670/oceanog.2009.71, 2009.

Hernandez, F., Smith, G., Baetens, K., Cossarini, G., Garcia-Hermosa, I., Drevillon, M., et al.: Measuring Performances, Skill and Accuracy in Operational Oceanography: New Challenges and Approaches, New Frontiers in Operational Oceanography, E. Chassignet, A. Pascual, J. Tintoré, and J. Verron, Eds., GODAE OceanView, 759-796, doi:10.17125/gov2018.ch29, 2018.

Katsafados, P., Papadopoulos, A., Korres, G., and Varlas, G.: A fully coupled Atmosphere–Ocean Wave modeling system (WEW) for the Mediterranean Sea: interactions and sensitivity to the resolved scales and mechanisms, Geosci. Model Dev., 9, 161–173, 2016.

Kempe, S., Pettine M., and Cauwet, G.: Biogeochemistry of european rivers, In Degensempe & Richey eds, biogeochemistry of Major World Rivers, SCOPE 42 John Wiley 169-211, 1991.

Komen, G.J., Hasselmann, S., and Hasselmann, K.: On the existence of a fully developed windsea spectrum, J. Phys. Ocean., 14, 1271-1285, 1984.

Komen, G. J., Cavaleri, L., Donelan, M., Hasselmann, K., Hasselmann, S., and Janssen, P.: Dynamics and modelling of ocean waves, Cambridge University Press, Cambridge, 1994.

970

971 Korres, G., Papadopoulos, A., Katsafados, P., Ballas, D., Perivoliotis, L., and Nittis, K.: A 2-year intercomparison of the
972 WAM-Cycle4 and the WAVEWATCH-III wave models implemented within the Mediterranean Sea, Mediterranean Marine
973 Science, 12(1), 129-152, Mediterranean Marine Science, 12(1), 129–152.
974 https://doi.org/10.12681/mms.57https://doi.org/10.12681/mms.57, 2011.

975

976 Krasakopoulou, E., Souvermezoglou, E., Giannoudi, L., and Goyet, C.: Carbonate system parameters ad anthropogenic CO_2
977 in the North Aegean Sea during October 2013. Continental Shelf Research, 149, 69-81, 2017.

978

979 Lazzari, P., Teruzzi, A., Salon, S., Campagna, S., Calonaci, C., Colella, S., Tonani, M., and Crise, A.: Pre-operational short-
980 term forecasts for the Mediterranean Sea biogeochemistry, Ocean Sci., 6, 25–39, https://doi.org/10.5194/os-6-25-2010, 2010.

981

982 Lazzari, P., Solidoro, C., Ibello, V., Salon, S., Teruzzi, A., Branger, K., Colella, S., and Crise, A.: Seasonal and inter-annual
983 variability of plankton chlorophyll and primary production in the Mediterranean Sea: a modelling approach, Biogeosciences
984 2012, 9:217–233, doi:10.5194/bg-9-217-2012, 2012.

985

986 Lazzari, P., Solidoro, C., Salon, S., and Bolzon, G.: Spatial variability of phosphate and nitrate in the Mediterranean Sea: a
987 modelling approach, Deep-Sea Res. Pt. I, 108, 39–52, https://doi.org/10.1016/j.dsr.2015.12.006, 2016.

988

989 Lazzari, P., Álvarez, E., Terzić, E., Cossarini, G., Chernov, I., D'Ortenzio, F., and Organelli, E.: CDOM Spatiotemporal
990 Variability in the Mediterranean Sea: A Modelling Study, J. Mar. Sci. Eng., 9(2), 176, 2021.

991

992 Lionello, P., H. Gunther, and P. A. E. M., Janssen: Assimilation of altimeter data in a global third generation wave model, J.
993 Geophys. Res., 97C, 14 453–14 474, 1992.

994

995 Lellouche, J.-M., Greiner, E., Le Galloudec, O., Garric, G., Regnier, C., Drevillon, M., et al.: Recent updates on the
996 Copernicus Marine Service global ocean monitoring and forecasting real-time 1/12° high resolution system, Ocean Sci.
997 Discuss. doi: https://doi.org/10.5194/os-2018-15, 2018.

998

999 Lermusiaux, O.F.J.: Evolving the subspace of the three-dimensional multiscale ocean variability: Massachusetts Bay, Journal
1000 of Marine Systems 29, 385–422, https://doi.org/10.1016/S0924-7963(01)00025-2 2001.

1001

1002 Le Traon, P. Y., Reppucci, A., Alvarez Fanjul, E., Aouf, L., Behrens, A., Belmonte, M., et al.: From Observation to
1003 Information and Users: The Copernicus Marine Service Perspective, Front. Mar. Sci. 6:234. doi: 10.3389/fmars.2019.00234,
1004 2019.

1005

1006 Levy, M., Estubier, A., and Madec, G.: Choice of an advection scheme for biogeochemical models. Geophys. Res. Let., 28.
1007 Madec, G. and the NEMO system Team, NEMO Ocean Engine, Scientific Notes of Climate Modelling Center (27) - ISSN
1008 1288-1619, Institut Pierre-Simon Laplace (IPSL) 2019, http://doi.org/10.5281/zenodo.1464816 2001

1009

1010 Madec, G., Delecluse, P., Imbard, M., and Levy, C.: OPA8.1 Ocean general Circulation Model reference m anual. Note du
1011 Pole de modelisazion, Institut Pierre-Simon Laplace (IPSL), France, 11, 1998.

1012

1013 Maderich, V., Ilyin, Y., and Lemeshko, E.: Seasonal and interannual variability of the water exchange in the Turkish Straits
1014 System estimated by modelling, Mediterr. Mar. Sci., [S.l.], v. 16, n. 2, p. 444-459, ISSN 1791-6763,
1015 doi:http://dx.doi.org/10.12681/mms.1103, 2015.

1016

1017 Mannarini, G. and Carelli, L.: VISIR-1. b: Ocean surface gravity waves and currents for energy-efficient navigation,
1018 Geoscientific Model Development, 12(8), 3449-3480, 2019.

1019 Marchesiello, P., McWilliams, JC., and Shchepetkin, A.: Open boundary conditions for long-term integration of regional
1020 oceanic models, Ocean modelling, 3.1–2, pp. 1–20, 2001.

McEwan, R., Kay, S., and Ford, D.: Quality Information Document of NWSHELF_ANALYSISFORECAST_BGC_004_002. Marine Copernicus Service. https://catalogue.marine.copernicus.eu/documents/QUID/CMEMS-NWS-QUID-004-002.pdf, accessed 15 July 2022, 2021.

McGovern, J.V., Dabrowski, T., Pereiro, D., Gutknecht, E., Lorente, P., Reffray, G., Aznar, R., and Sotillo, M.G.: Quality Information Document of IBI_ANALYSISFORECAST_BGC_005_004. Marine Copernicus Service. https://catalogue.marine.copernicus.eu/documents/QUID/CMEMS-IBI-QUID-005-004.pdf, accessed 15 July 2022, 2020.

Melsom, A. and Yumruktepe, Ç.: Quality Information Document of ARTIC_ANALYSIS_FORECAST_BIO_002_004. Marine Copernicus Service. https://catalogue.marine.copernicus.eu/documents/QUID/CMEMS-ARC-QUID-002-004.pdf, accessed 15 July 2022, 2021.

Meybeck, M. and Ragu, A.: River Discarges to the Oceans: An Assessment of suspended solids, major ions and nutrients UNEP STUDY, 1995.

Milliff, R., Bonazzi, A., Wikle, C.K., Pinardi, N., and Berliner, L. M.: Ocean ensemble forecasting. Part I: Ensemble Mediterranean winds from a Bayesian hierarchical model, Q. J. R. Meteorol. Soc. 137: 858–878. DOI:10.1002/qj.767, 2011.

Nagy, H., Lyons, K., Nolan, G., Cure, M., and Dabrowski, T.: A Regional Operational Model for the North East Atlantic: Model Configuration and Validation, J. Mar. Sci. Eng., 8, 673. https://doi.org/10.3390/jmse8090673, 2020.

Napolitano, E., Iacono, R., Palma, M., Sannino, G., Carillo, A., Lombardi, E., Pisacane, G. and Struglia, M.V.: MV (2022) MITO: A new operational model for the forecasting of the Mediterranean sea circulation,. Front. Energy Res. 10:941606. doi: 10.3389/fenrg.2022.941606, 2022.

Oddo, P., Adani, M., Pinardi, N., Fratianni, C., Tonani, M., and Pettenuzzo, D.: A Nested Atlantic-Mediterranean Sea General Circulation Model for Operational Forecasting, Ocean Sci., 5, 461-473, doi:10.5194/os-5-461-2009, 2009.

Oddo, P., Bonaduce, A., Pinardi, N., and Guarnieri, A.: Sensitivity of the Mediterranean sea level to atmospheric pressure and free surface elevation numerical formulation in NEMO, Geosci. Model Dev., 7, 3001–3015. doi:10.5194/gmd-7-3001-2014, 2014.

Orlanski, I.: A simple boundary condition for unbounded hyperbolic flows,". Journal of computational physics, 21.3, pp. 251–269, 1976.

Pacanowski, R. C., and Philander, S. G. H.: Parameterization of vertical mixing in numerical models of tropical oceans. Journal of Physical Oceanography, 11, 1443–1451. https://doi.org/10.1175/1520-0485(1981)011<1443:POVMIN>2.0.CO;2, 1981.

Pettenuzzo, D., Large, W. G., and Pinardi, N.: On the corrections of ERA-40 surface flux products consistent with the Mediterranean heat and water budgets and the connection between basin surface total heat flux and NAO, J. Geophys. Res., 115 (C6), doi:10.1029/ 2009JC005631, URL http://dx.doi.org/10.1029/2009JC005631, 2010.

Pinardi, N., Arneri, E., Crise, A., Ravaioli, M., and Zavatarelli, M.: "The physical, sedimentary and ecological structure and variability of shelf areas in the Mediterranean Sea" The Sea, Vol. 14 (A. R. Robinson and K. Brink Eds.), Harvard University Press, Cambridge, USA 1243-1330, 2006.

Pinardi, N., and Coppini, G.: Preface "Operational oceanography in the Mediterranean Sea: the second stage of development", Ocean Sci., 6, 263–267, https://doi.org/10.5194/os-6-263-2010, 2010.

Pinardi, N., Zavatarelli, M., Adani, M., Coppini, G., Fratianni, C., Oddo, P., et al.: Mediterranean Sea large-scale low-frequency ocean variability and water mass formation rates from 1987 to 2007: A retrospective analysis, Prog. Oceanogr, 132, 318–332, https://doi.org/10.1016/j.pocean.2013.11.003, 2015.

1073
1074 Pinardi, N., Lermusiaux, P., F. J.; Brink Kenneth, H., Preller Ruth, H.: The Sea: The science of ocean predictions. Journal of
1075 Marine Research, Volume 75, Number 3, May 2017, pp. 101-102(2), 10.1357/002224017821836833, 2017.
1076
1077 Pinardi, N., Cessi, P., Borile, F., and Wolfe, C.L.: The Mediterranean Sea Overturning Circulation, J. Phys. Oceanogr., 49,
1078 1699–1721, doi: 10.1175/JPO-D-18-0254.1, 2019.
1079
1080 Pineau-Guillou, L., Ardhuin, F., Bouin, M.-N., Redelsperger, J.-L., Chapron, B., Bidlot, J.-R., and Quilfen Y.: Strong winds
1081 in a coupled wave-atmosphere model during a North Atlantic storm event: evaluation against observations, Quarterly Journal
1082 of the Royal Meteorological Society, 144(711), Part B, 317-332.
1083 https://doi.org/10.1002/qj.3205https://doi.org/10.1002/qj.3205, 2018.
1084
1085 Pistoia, J., Clementi, E., Delrosso, D., Mattia, G., Fratianni, C., Drudi, M., et al.: Last improvements in the data assimilation
1086 scheme for the Mediterranean Analysis and Forecast system of the Copernicus Marine Service, Extended abstract to the 8th
1087 EuroGOOS Conference 2017, Bergen, http://eurogoos.eu/download/publications/EuroGOOS-2017-Conference-
1088 Proceedings.pdf, 2017.
1089
1090 Ramirez-Romero, E., Jordà, G., Amores, A., Kay, S., Segura-Noguera, M., Macias, D.M., Maynou, F., Sabatés, A., and
1091 Catalán, I.A.: Assessment of the Skill of Coupled Physical–Biogeochemical Models in the NW Mediterranean, Front. Mar.
1092 Sci. 7:497. doi: 10.3389/fmars.2020.00497, 2020.
1093
1094 Ravdas, M., Zacharioudaki, A., and Korres, G.: Implementation and validation of a new operational wave forecasting system
1095 of the Mediterranean Monitoring and Forecasting Centre in the framework of the Copernicus Marine Environment
1096 Monitoring Service, Nat. Hazards Earth Syst. Sci., 18, 2675-2695, https://doi.org/10.5194/nhess-18-2675-2018, 2018.
1097
1098 Ribera d'Alcalà, M., Civitarese, G., Conversano, F., and Lavezza, R.: Nutrient ratios and fluxes hint at overlooked processes
1099 in the Mediterranean Sea, Journal of Geophysical Research, 108(C9), 8106, doi:10.1029/2002JC001650, 2003.
1100
1101 Robinson, A.R., Leslie, W.G., Theocharis, A., and Lascartos, A.: Mediterranean Sea Circulation. Encyclopedia of Ocean
1102 Sciences, pp 1689-1705, https://doi.org/10.1006/rwos.2001.0376, 2001.
1103 Lazzari, P., Teruzzi, A., Solidoro, C., Crise, A.: Marine Ecosystem forecasts: skill performance of the CMEMS
1104 Mediterranean Sea model system. Ocean Sci. Discuss., 1–35, https://doi.org/10.5194/os-2018-145, 2019.
1105
1106 Salon, S., Cossarini, G., Bolzon, G., Feudale, L., Lazzari, P., Teruzzi, A., et al.: Novel metrics based on Biogeochemical
1107 Argo data to improve the model uncertainty evaluation of the CMEMS Mediterranean marine ecosystem forecasts,. Ocean
1108 Science, 15(4), 997-1022, 2019.
1109
1110 Schneider, A., Wallace, D. W. R., and Kortzinger, A.: Alkalinity of the Mediterranean Sea, Geophys. Res. Lett., 34, L15608,
1111 doi:10.1029/2006GL028842, 2007.
1112
1113 Schmechtig, C., Poteau, A., Claustre, H., D'Ortenzio, F., Dall'Olmo, G., and Boss, E.: Processing Bio-Argo particle
1114 backscattering at the DAC level, https://doi.org/10.13155/39468, 2018.
1115
1116 Semedo, A., Sušelj, K, Rutgersson, A., and Sterl, A.: A global view on the wind sea and swell climate and variability from
1117 EERA-40, J. Clim. 24 1461–79, 2011.
1118
1119 Simoncelli, S., Masina, S., Axell, L., Liu, Y., Salon, S., Cossarini, G., et al.: MyOcean regional reanalyses: overview of
1120 reanalyses systems and main results, Mercator Ocean J 54: Special issue on main outcomes of the MyOcean2 and MyOcean
1121 follow-on projects. https://www.mercator-ocean.fr/wpcontent/uploads/2016/03/JournalMO-54.pdf , 2016.
1122
1123 Simoncelli, S., Fratianni, C., Pinardi, N., Grandi, A., Drudi, M., Oddo, P., and Dobricic, S.: Mediterranean Sea Physical
1124 Reanalysis (CMEMS MED-Physics) (Version 1) [Data set], Copernicus Monitoring Environment Marine Service
1125 (CMEMS), https://doi.org/10.25423/MEDSEA_REANALYSIS_PHYS_006_004, 2019.

1126
1127 Siokou-Frangou, I., Christaki, U., Mazzocchi, M.G., Montresor, M., Ribera d'Alcal, M., Vaqu, D., and Zingone, A.:
1128 Plankton in the open Mediterranean Sea: a review, Biogeosciences, 7 (5):1543–1586, 2010.
1129
1130 Snyder, R. L., Dobson, F. W., Elliot, J. A., and Long, R. B.: Array measurements of atmospheric pressure fluctuations above
1131 surface gravity waves, J. Fluid Mech., 102, 1–59, 1981.
1132
1133 Sotillo, M. G., Garcia-Hermosa, I., Drévillon, M., Régnier, C., Szczypta, C., Hernandez, F., Melet, A., and Le Traon, P.Y.:
1134 Communicating CMEMS Product Quality: evolution & achievements along Copernicus-1 (2015- 2021), Mercator Ocean
1135 Journal #57, https://marine.copernicus.eu/it/node/19306https://marine.copernicus.eu/it/node/19306, 2021.
1136
1137 Souvermezoglou, E., Krasakopoulou, E., and Pavlidou, A.: Temporal and spatial variability of nutrients and oxygen in the
1138 North Aegean Sea during the last thirty years. Mediterranean Marine Science, 15/4, 805-822, 2014.
1139
1140 Spruch L ., Verjovkina, S., Jandt, S., Schwichtenberg, F., Huess, V., Lorkowski, I., and Lagemaa, P.: Quality Information
1141 Document of BALTICSEA_ANALYSIS_FORECAST_BIO_003_007. Marine Copernicus Service.
1142 https://catalogue.marine.copernicus.eu/documents/QUID/CMEMS-BAL-QUID-003-007.pdf, accessed 15 July 2022, 2020.
1143
1144 Storto, A., Masina, S., and Navarra, A.: Evaluation of the CMCC eddy-permitting global ocean physical reanalysis system
1145 (C-GLORS, 1982-2012) and its assimilation components, Quarterly Journal of the Royal Meteorological Society, 142, 738–
1146 758, doi: 10.1002/qj.2673, 2015.
1147
1148 Taburet, G., Sanchez-Roman, A., Ballarotta, M., Pujol, M.-I., Legeais, J.-F., Fournier, F.; Faugere, Y., and Dibarboure, G.:
1149 DUACSDT2018: 25years of reprocessed sea level altimetry products, Ocean Sci., 15, 1207–1224,
1150 https://doi.org/10.5194/os-15-1207-2019, 2019.
1151
1152 Terzic, E., Salon, S., Solidoro, C., Cossarini, G., Teruzzi, A., Miro, A., and Lazzari. P.: Impact of interannually variable
1153 diffuse attenuation coefficients for downwelling irradiance on biogeochemical modelling, Ocean Modell., OCEMOD-D-20-
1154 00012R2, 2021.
1155
1156 Teruzzi, A., Dobricic, S., Solidoro, C., and Cossarini, G.: A 3D variational assimilation scheme in coupled transport
1157 biogeochemical models: Forecast of Mediterranean biogeochemical properties, J. Geophys. Res. Oceans, 119, 200–217,
1158 https://doi.org/10.1002/2013JC009277, 2014.
1159
1160 Teruzzi, A., Bolzon, G., Salon, S., Lazzari, P., Solidoro, C., and Cossarini, G.: Assimilation of coastal and open sea
1161 biogeochemical data to improve phytoplankton modelling in the Mediterranean Sea, Ocean Model. 132, 46–60,
1162 https://doi.org/10.1016/j.ocemod.2018.09.007, 2018.
1163
1164 Teruzzi, A., Di Cerbo, P., Cossarini, G., Pascolo, E., and Salon, S.: Parallel implementation of a data assimilation scheme for
1165 operational oceanography: the case of the OGSTM-BFM model system, Comput. Geosci., 124, 103–114,
1166 https://doi.org/10.1016/j.cageo.2019.01.003, 2019.
1167
1168 Teruzzi, A., Bolzon, G., Feudale, L., and Cossarini, G.: Deep chlorophyll maximum and nutricline in the Mediterranean Sea:
1169 emerging properties from a multi-platform assimilated biogeochemical model experiment, Biogeosciences, 18(23), 6147-
1170 6166, 2021.
1171
1172 Thoppil, P.G., Frolov, S., Rowley, C.D., Reynolds C. A., Jacobs G. A., E. Metzger J., et al.: Ensemble forecasting greatly
1173 expands the prediction horizon for ocean mesoscale variability, Commun Earth Environ 2, 89
1174 https://doi.org/10.1038/s43247-021-00151-5, 2021.
1175
1176 Toledano, C., Ghantous, M., Lorente, P., Dalphinet, A., Aouf, L., and Sotillo, M.G.: Impacts of an Altimetric Wave Data
1177 Assimilation Scheme and Currents-Wave Coupling in an Operational Wave System: The New Copernicus Marine IBI Wave
1178 Forecast Service, J. Mar. Sci. Eng.10, 457, https://doi.org/10.3390/jmse10040457, 2022.

1179
1180 Tonani, M., Balmaseda, M., Bertino, L., Blockley, E., Brassington, G., Davidson, F., et al.: Status and future of global and
1181 regional ocean prediction systems, J Operational Oceanography 8:201-220, doi:10.1080/1755876X.2015.1049892, 2015.
1182
1183 Tonani, M., Pinardi, N., Dobricic, S., Pujol, I., and Fratianni, C.: A high-resolution free-surface model of the Mediterranean
1184 Sea, Ocean Sci., 4, 1-14, 2008.
1185
1186 Trisolino, P., di Sarra, A., Sferlazzo, D., Piacentino, S.; Monteleone, F., Di Iorio, T., et al.: Application of a Common
1187 Methodology to Select in Situ CO_2 Observations Representative of the Atmospheric Background to an Italian Collaborative
1188 Network, Atmosphere, 12, 246. https://doi.org/10.3390/atmos12020246, 2021.
1189
1190 Tugrul, S., Besiktepe, T., and Salihoglu, I.: Nutrient exchange fluxes between the Aegean ad tBlack Seas through the
1191 Marmara Sea, Mediterranean Marine Science, 3/1, 33-42, 2002.
1192
1193 Vandenbulcke L., Capet A., and Grégoire M.: Quality Information Document of
1194 BLKSEA_ANALYSIS_FORECAST_BIO_007_010, Marine Copernicus Service,
1195 https://catalogue.marine.copernicus.eu/documents/QUID/CMEMS-BS-QUID-007-010.pdf, accessed 15 July 2022, 2021.
1196
1197 Verri, G., Pinardi, N., Bryan, F., Tseng, Y., Coppini, G., and Clementi, E.: A box model to represent estuarine dynamics in
1198 mesoscale resolution ocean models, Ocean Modelling. http://dx.doi.org/10.1016/j.ocemod.2020.101587
1199 http://dx.doi.org/10.1016/j.ocemod.2020.101587, 2020.
1200
1201 Vichi M., Lovato, T., Butenschön, M., Tedesco, L., Lazzari, P., Cossarini, G., et al.: The Biogeochemical Flux Model
1202 (BFM): Equation Description and User Manual, BFM version 5.2. BFM Report series N. 1, Release 1.2, June 2020,
1203 Bologna, Italy, http://bfm-community.eu, pp. 104, 2020.
1204
1205 Vichi, M., Lovato, T., Butenschön, M., Tedesco, L., Lazzari, P., Cossarini, G., Masina, S., Pinardi, N., Solidoro, C., and
1206 Zavatarelli, M.: The Biogeochemical Flux Model (BFM): Equation Description and User Manual. BFM version 5.2. BFM
1207 Report series N. 1, Release 1.2, June 2020, Bologna, Italy, http://bfm-community.eu, pp. 104, 2020.
1208
1209 Volpe, G., Colella, S., Brando, V. E., Forneris, V., Padula, F. L., Cicco, A. D., et al.: Mediterranean ocean colour Level 3
1210 operational multi-sensor processing, Ocean Science, 15(1), 127-146, 2019.
1211
1212 von Schuckmann, K., Le Traon, P.-Y., Alvarez Fanjul, E., Axell, L., Balmaseda, M., Breivik, L.-A., et al.: The Copernicus
1213 Marine Environment Monitoring Service Ocean State Report, Journal of Operational Oceanography, 9:sup2, s235-s320,
1214 DOI: 10.1080/1755876X.2016.1273446, 2016.
1215
1216 von Schuckmann K., Le Traon, P.-Y., Smith, N., Pascual, A., Brasseur, P., Fennel, K., et al.: Copernicus Marine Service
1217 Ocean State Report, Journal of Operational Oceanography, 11:sup1, S1-S142, DOI: 10.1080/1755876X.2018.1489208,
1218 2018.
1219
1220 von Schuckmann K., Le Traon, P.-Y., Smith, N., Pascual, A., Djavidnia, S., Gattuso, J.-P., et al.: Copernicus Marine Service
1221 Ocean State Report, Issue 3, Journal of Operational Oceanography, 12:sup1, S1-S123, DOI:
1222 10.1080/1755876X.2019.1633075, 2019
1223
1224 von Schuckmann, K., Le Traon, P.-Y., Smith, N., Pascual, A., Djavidnia, S., Gattuso, J.-P., et al.: Copernicus Marine Service
1225 Ocean State Report, Issue 4. J.Op. Oceanogr., 13, https://doi.org/10.1080/1755876X.2020.1785097, 2020.
1226
1227 Zodiatis, G., Lardner, R., Lascaratos, A., Georgiou, G., Korres, G., and Syrimis, M.: High resolution nested model for the
1228 Cyprus, NE Levantine Basin, eastern Mediterranean Sea: implementation and climatological runs, Ann. Geophys., 21, 221–
1229 236, https://doi.org/10.5194/angeo-21-221-2003, 2003.
1230

1231   WAMDI Group. The WAM model—a third generation ocean wave prediction model, J. Phys. Oceanogr., 18:1775–1810.
1232   https://doi.org/10.1175/1520-0485(1988)018<1775:TWMTGO>2.0.CO;2, 1988.
1233
1234   Wanninkhof, R.: Relationship between wind speed and gas exchange over the ocean revisited, Limnol. Oceanogr. Methods
1235   12, 351–362. https://doi.org/10.4319/lom.2014.12.351, 2014.
1236
1237   Weatherall, P., Marks, K. M., Jakobsson, M., Schmitt, T., Tani, S., Arndt, J. E., Rovere, M., Chayes, D., Ferrini, V. and
1238   Wigley, R.: A new digital bathymetric model of the world's oceans, Earth and space Science, 2(8), 331-345, 2015.
1239
1240   Yalcin, B., Artuz, M.L., Pavlidou, A., Cubuk, S., and Dassenakis, M.: Nutrient dynamics and eutrophication in the Sea of
1241   Marmara: data from recent oceanographic research. Science of the Total Environment, 601-602, 405-424, 2017.
1242
1243   Young, I.R.: Seasonal variability of the global ocean wind and wave climate, Int. J. Climatol. 19, 931–950.
1244   doi:10.1002/(SICI)1097-0088(199907)19:93.0.CO;2-O, 1999.
1245
1246

1248
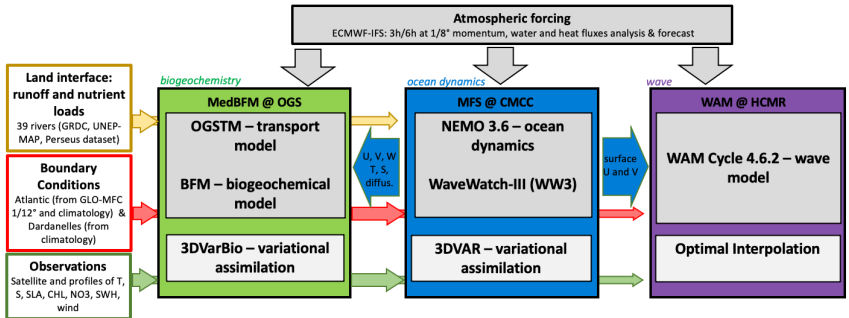
1249

1250 **Figure 1: The Med-MFC core components and the off-line coupling scheme. The Blue arrow are the exchanged fields at daily**
1251 **frequency between the three components.**

1252
1253
1254

1255
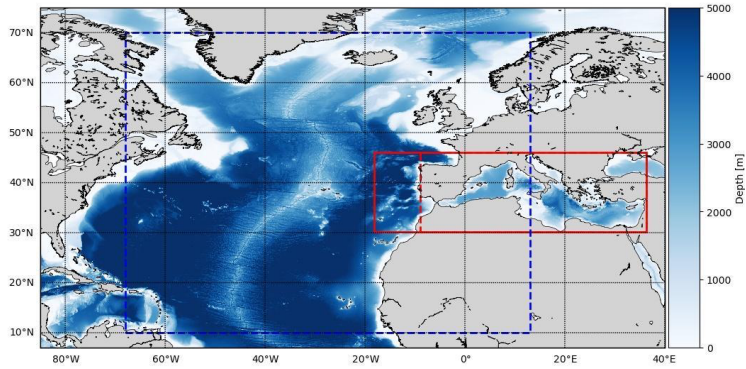
1256

1257 **Figure 2. The solid red box presents the domain of the PHY and WAV Mediterranean components. For BIO the domain extends in**
1258 **the Atlantic as far as the dashed red line. The blue box presents one of the WAM domains, producing boundary conditions for the**
1259 **Mediterranean WAV component which extends only in the solid red box.**

1260
1261
1262
1263
1264
1265
1266
1267
1268
1269
1270
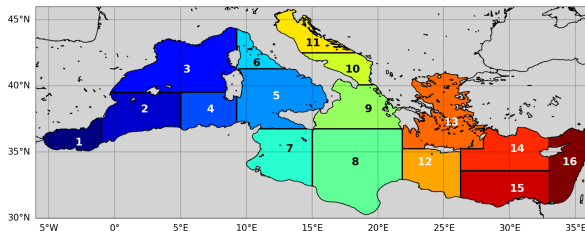
1271
1272 **Figure 3 The Mediterranean Sea domain and sub-regions subdivision for analysis of the skill scores: Alboran (1), South-West**
1273 **Mediterranean-1 (2), North-West Mediterranean (3), South-West Mediterranean-2 (4), South Tyrrenian (5), North Tyrrenian (6),**
1274 **West Ionian (7), East Ionian (8), North-East Ionian (9), South Adriatic (10), North Adriatic (11), West Levantine (12), Aegean (13),**
1275 **North-Central Levantine (14), South-Central Levantine (15), East Levantine (16).**

1276
1277
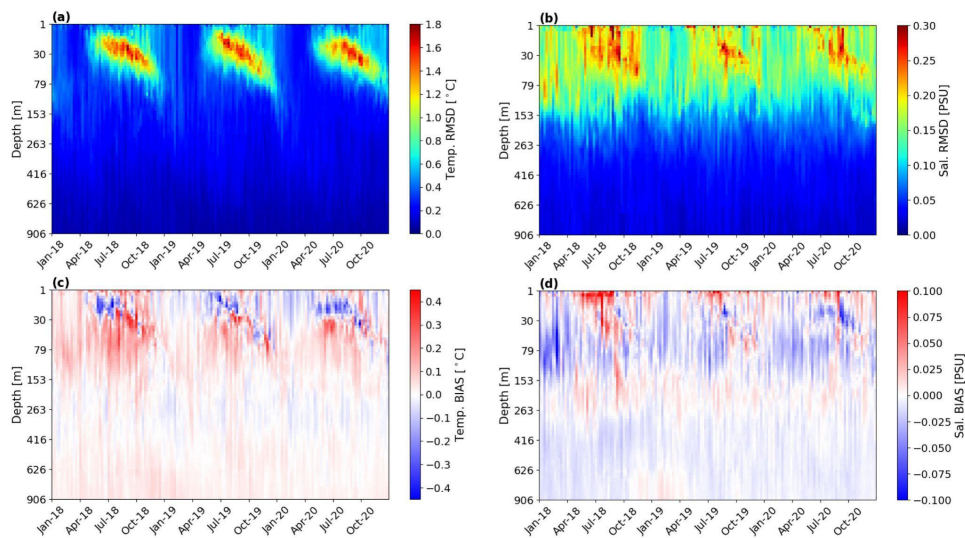
1278

1279 **Figure 4 Hovmöller (Depth-Time) diagrams: (a) weekly RMS of temperature misfits, (b) weekly RMS salinity misfits, (c) weekly**
1280 **bias of temperature and (d) weekly bias of salinity, evaluated along the water column and averaged in the whole Mediterranean Sea.**

1281

1282

1283
1284
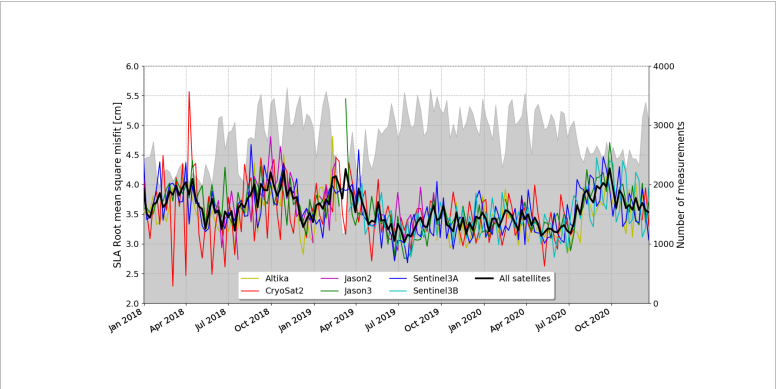
1285 **Figure 5. Time Series of weekly mean RMS misfit error for SLA evaluated with respect to available satellite altimeters and averaged**

1286 **in the whole Mediterranean Sea. Black bold line represents the mean error with respect to the whole set of satellites which are**

1287 **separately shown with different colours. The grey area indicates the number of observations used for the validation.**
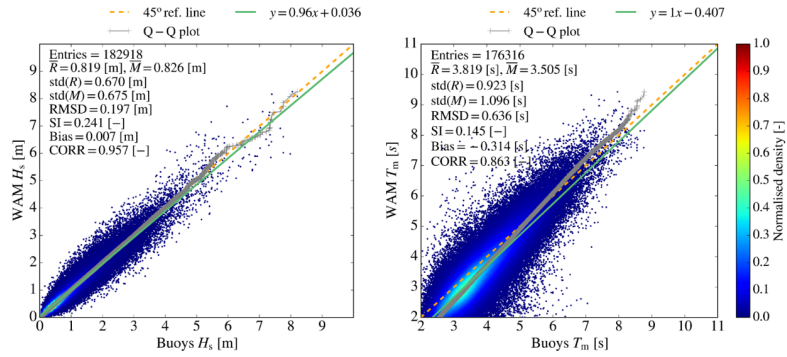
1289
1290 **Figure 6. Scatter plots of: (left) significant wave height (Hs); (right) mean wave period (Tm) versus wave buoy observations, for the**
1291 **28 stations of the Mediterranean Sea (bottom panel of Figure 7), for a three-year period (2018-2020). The graphs also include**
1292 **quantile-quantile plots (grey crosses), 45° reference lines (dashed orange line), and least-squares best fit lines (green line). On the**
1293 **top left of each picture statistical scores are given: entries refer to the number of data available for computing the statistics, R, M**
1294 **refer to the observed and modelled value respectively, SI is the Scatter Index (defined as the standard deviation of model-observation**
1295 **differences relative to the observed mean), and CORR is the Pearson correlation coefficient.**

1296
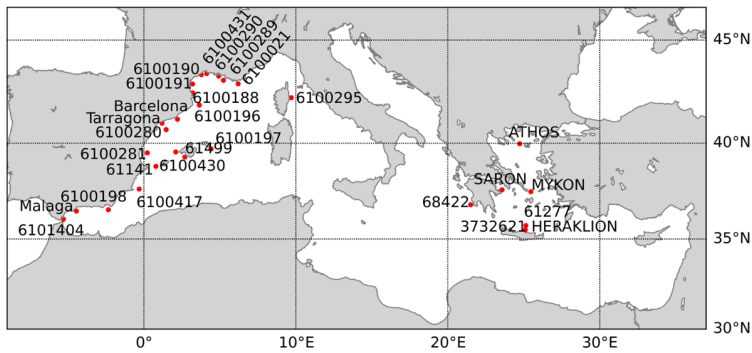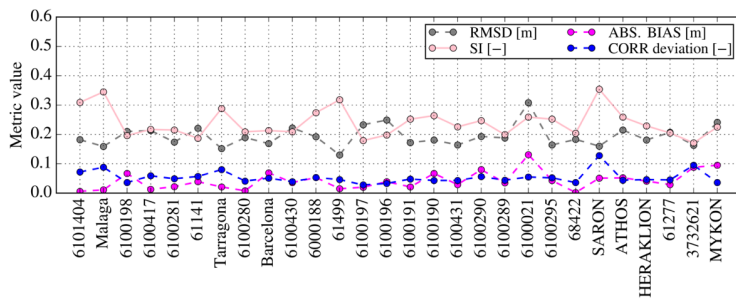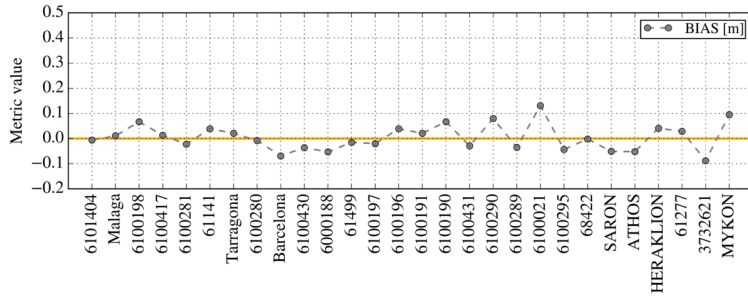
1297

Figure 7. Significant wave height difference between model and observations (upper and middle graph) at the 28 buoy locations (lower panel) for a three-year period (2018-2020). For all locations, the performance of the model is evaluated against buoy data by means of bias, root mean square difference (RMSD), Scatter Index (SI), and deviations of the Pearson correlation coefficient from unity (CORR deviation).
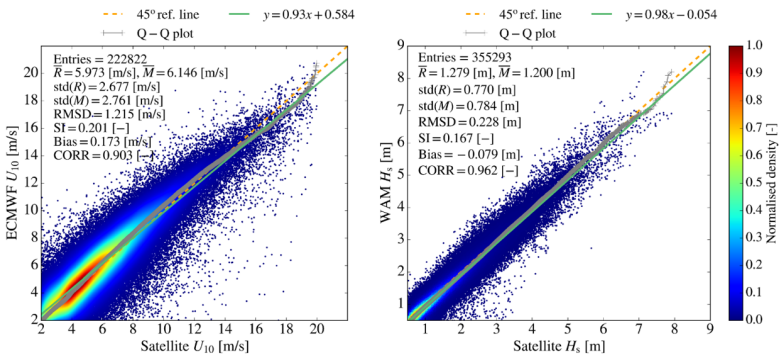
Figure 8. Scatter plots of: ECMWF forcing wind speed U10 versus satellite U10 observations (left) and model significant wave height (Hs) versus satellite observations over the entire Mediterranean basin, for the three-year period (2018 – 2020).

SI [-]
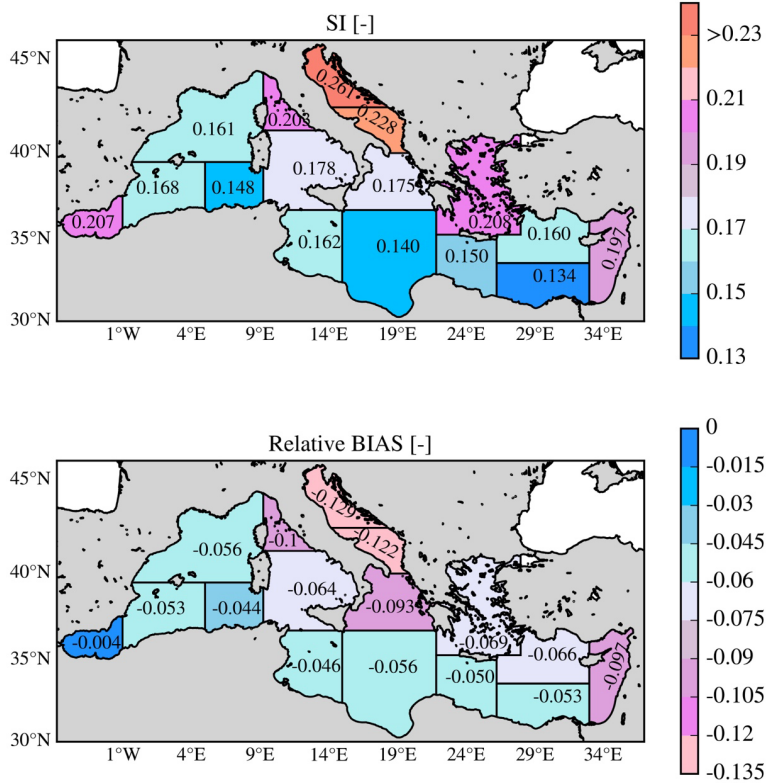
Relative BIAS [-]

1319
1320 **Figure 9. SWH evaluation against satellite data: maps of Scatter Index (SI) (top) and Relative BIAS (bottom) over the Mediterranean**
1321 **Sea sub-regions (shown in Figure 3) for the three-year period (2018-2020).**

1322
1323
1324
1325
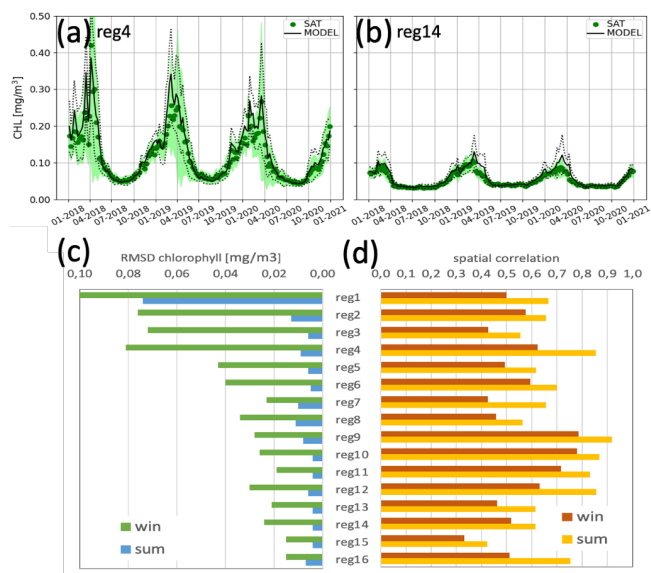
1331 **Figure 10. Timeseries of surface chlorophyll for centred composite 7-day satellite (green) and the model analysis (black) in two**
1332 **selected sub-regions (a and b). RMS of differences (c) and Pearson correlation (d) between maps of satellite and model forecast for**
1333 **the day before the assimilation in the 16 sub-regions of Figure Fig.5(c). Metrics are averaged over the winter (from Oct to Apr) and**
1334 **summer (from May to September) periods.**

1335

1336

1341
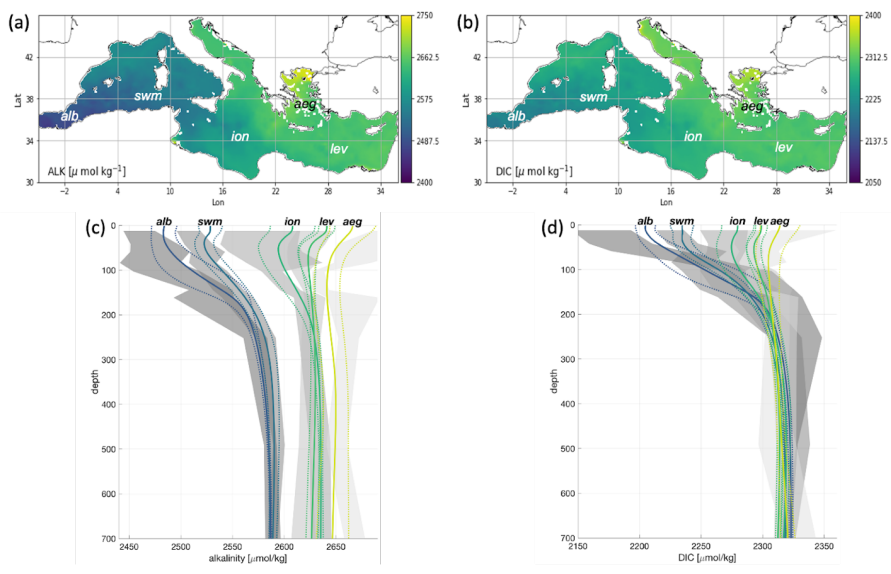
Figure 11. Spatial distribution of modelled DIC (a) and alkalinity (b) and comparison of vertical profiles of DIC (c) and alkalinity (d) for model (average and range of variability, solid and dashed coloured lines, respectively) and Emodnet climatology (average and range of variability, black dots and lines and grey shaded areas, respectively) for selected macro areas. Climatological data are computed using historical data (Emodnet, 2018; Bakker 2014). The range of variability is the average ± standard deviation

1346
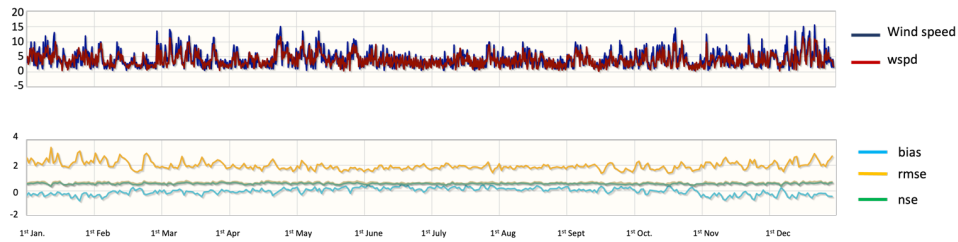
1347

Figure 12: Example of ECMWF wind speed validation with respect to METAR ground observations in 2019 in the area of the Gulf of Lion. Top panel: time series of daily mean wind speed time series from METAR station (blue line) and from ECMWF (red line). Bottom panel: time series of main skill metrics (bias, RMS Error (RMSE), Nash-Sutcliffe Model Efficiency Coefficient (nse)).

Tables

1355   Table 1 Changes in the Mediterranean forecasting components since 2008.

Year	Numerical Model Changes
Physics component (PHY)	
< 2008	1/16 deg., 72 vert. lev., OPA8.2 model (Madec et al., 1998) with closed lateral boundary conditions in the Atlantic (Tonani et al., 2008), 7 rivers (Ebro, Rhone, Nile, Po, Seman, Vjiose, Buna-Bojana), closed lateral boundary at Dardanelles strait, OceanVar (Dobricic et al., 2007) weekly assimilation
2009	As in 2008 with NEMOv3.1 with climatological lateral open boundary conditions in the Atlantic (Oddo et al., 2009), OceanVar with daily assimilation (Dobricic et al., 2007)
2010	As in 2009 with one-way offline coupling between NEMOv3.1 and WAM (wave)
2013	As in 2010 with two-way coupling between NEMOv3.4 and WW3 (Clementi et al., 2017a)
2014	As in 2013 but with surface atmospheric pressure forcing (Oddo et al., 2014), explicit linear free surface and SLA TAPAS(*) data assimilation (Dobricic et al., 2012)
2015	As in 2014 but with daily lateral open boundary conditions in the Atlantic
2016	As in 2015 but with monthly and grid point EOF and vertical observational error varying with depth in OceanVar
2017	1/24 deg., 141 vert. lev., NEMOv3.6 with nonlinear free surface and z-star coordinate system), 39 rivers (Table A.4)
2019	As in 2017 but with open lateral boundary conditions at the Dardanelles Strait, improved SST nudging
Biogeochemistry component (BIO)	
<2008	1/8 deg BFM offline coupled to PHY component
2009	Offline coupling to horizontal subsampled PHY component at 1/8 deg
2013	Coupling with 1/16 deg PHY component and Biogeochemical Data Assimilation (BDA) for Ocean Color derived Chlorophyll data (Teruzzi et al., 2014)
2015	Inclusion of the carbonate system in the model (Cossarini et al., 2015)
2017	Revision nutrient formulation in BFM (Lazzari et al., 2016) and coupling with 1/24 deg PHY component including z-star coordinate system
2018	BDA for Ocean Color coastal data (Teruzzi et al., 2018)
2019	Open lateral boundary condition at the Dardanelles Strait, revision daily light cycle in BFM (Salon et al., 2019)
2020	Open lateral boundary condition in the Atlantic Ocean and BDA with Argo biogeochemical data (Cossarini et al., 2019), and daily operational 10-days of forecast
Wave component (WAV)	
2017	1/24 deg WAM Cycle 4.5.4, one-way offline coupled to PHY component surface currents. Open boundary conditions from North Atlantic implementation of WAM model at 1/6 deg resolution.
2018	Implementation of data assimilation for along track Significant Wave Height (SWH) observations from Jason 3 and Sentinel 3a

2019	WAM Cycle 4.6.2; assimilation of Cryosat-2 and Saral/Altika SWH observations tuning of wave age parameter; imposition of a limitation to the high frequency part of the spectrum based on Phillips spectrum.
2020	Assimilation of Sentinel-3b SWH observations t

(*) the Sea Level Anomaly (SLA) TAPAS product is produced to give information about the different corrections of the altimetric original signal.

Table 2. EAN estimates with in-situ observations. The differences (BIAS) and their square values (RMSD) are then averaged over the whole Mediterranean Sea region and 9 vertical layers for years 2018-2020.

Layer (m)	Temperature RMSD (°C)	Temperature bias (°C)	Salinity RMSD (PSU)	Salinity bias (PSU)
0-10	0.54	-0.02	0.19	0.01
10-30	0.82	-0.04	0.20	-0.01
30-60	0.85	0.04	0.19	-0.01
60-100	0.58	0.03	0.16	-0.02
100-150	0.41	-0.01	0.13	-0.01
150-300	0.28	-0.02	0.08	0.00
300-600	0.18	0.00	0.05	-0.01
600-1000	0.09	-0.02	0.03	0.00
1000-2000	0.05	0.01	0.02	0.00

Table 3. Gibraltar mean and standard deviation volume transports [Sv] from the Med-PHY numerical system averaged in the period 2018-2020 compared to literature values (current meter observations from October 2004 to January 2009).

Gibraltar Transport	Model [2018-2020]	Literature Soto-Navaro et al. (2010) [2004-2009]	Literature Candela (2001) [1994-1996]
Net	0.040±0.017	0.038 ± 0.007	0.04 (max: 0.26, min: 0.11)
Eastward	0.91±0.01	0.81 ± 0.06	1.01 (max: 1.12, min: 0.91)
Westward	0.87±0.06	0.78 ± 0.05	0.97 (max: 0.83, min: 1.11)

1377

1378   Table 4. EAN RMSD and Bias of SST and SLA RMSD averaged in the whole Mediterranean Sea and 16 sub-regions (see Figure
1379   3) for the period 2018-2020.

Region	Temperature RMSD (°C)	Temp. Bias (°C)	Sea Level Anomaly RMSD (cm)
MED SEA	0.54	0.12	3.8
REGION 1	0.69	-0.05	5.3
REGION 2	0.53	0.06	4.3
REGION 3	0.53	-0.01	3.2
REGION 4	0.55	0.15	5.1
REGION 5	0.47	0.13	3.1
REGION 6	0.49	0.15	3.5
REGION 7	0.51	0.22	5.0
REGION 8	0.55	0.16	3.8
REGION 9	0.51	0.14	3.4
REGION 10	0.58	0.20	2.3
REGION 11	0.63	0.08	NA
REGION 12	0.49	-0.01	4.0
REGION 13	0.59	0.14	3.6
REGION 14	0.57	0.16	3.3
REGION 15	0.53	0.13	4.4
REGION 16	0.52	0.24	3.1

1380
1381
1382

1383

1384

1385

1386

1387

1388 Table 5. RMS of the difference between MedBFM and Argo-BGC profiles for ecosystem metrics. RMSD of the metrics are computed for
1389 each profile, then averaged over time and space considering the 2017-2020 period. Sub-regions: swm (reg2+reg4), nwm (reg3), tyr
1390 (reg5+reg6), adr (reg10+reg11), ion (reg7+reg8+reg9) and lev (reg13+reg14+reg15+reg16).

	vertical metrics [units]	mean value [range]	RMSD					
			swm	nwm	tyr	adr	ion	lev
Chlorophyll	Average 0-200 m [mg/m3]	[0.01 - 1.5]	0.05	0.06	0.06	0.03	0.03	0.03
	Deep chlorophyll maximum depth [m]	80 [60-130]	10	11	7	6	16	18
	Mixed Bloom Winter depth [m]	40 [20-90]	25	39	35	29	16	27
Nitrate	Average 0-200 m [mmol/m3]	[0.1-8.0]	-	0.72	0.45	-	0.52	0.54
	Nitracline depth [m]	90 [70-150]	-	48	44	-	34	42
Oxygen	Average 0-200 m [mmol/m3]	220 [190-250]	11.5	8.5	7.9	10.8	4.7	5.7
	Maximum oxygen depth [m]	[60-120]	24	16	17	19	34	14

1391
1392
1393
1394

1395
1396

1397 Table 6. RMSD of the difference between model and climatological profiles at different depths evaluated in the 2017-2020 reference period.
1398 Statistics are computed using the 16 sub-regions in Figure 3. Reference datasets for validation (last column) are: (1) EMODnet data
1399 collections (Buga et al., 2018) integrated with additional oceanographic cruises (Cossarini et al., 2015), and (2) Socat dataset (Baker et al
1400 2014).

1401

Variable	indicative range values	RMSD								data set
		0-10m	10-30m	30-60m	60-100m	100-150m	150-300m	300-600m	600-1000m	
Phosphate [mmol/m³]	0.01-0.70	0.03	0.03	0.027	0.023	0.043	0.028	0.040	0.027	1
Nitrate [mmol/m³]	0.1-9.0	0.42	0.41	0.49	0.72	0.83	0.72	1.09	0.83	1
Ammonia [mmol/m³]	0.01-1.23	0.41	0.17	0.15	0.23	0.30	0.32	0.44	0.54	1
Silicate [mmol/m³]	0.1-7.0	1.5	1.5	1.3	0.9	0.9	0.7	0.7	0.8	1
Oxygen [mmol/m³]	190-260	5.9	5.7	6.4	4.2	5.2	4.3	8.6	5.8	1
DIC [μmol/kg]	2100-2400	42.2	37.6	28.1	17.1	16.7	7.7	9.9	3.8	1
Alkalinity [μmol/kg]	2360-2730	41.7	34.4	26.0	19.1	12.5	12.1	9.0	7.0	1
pH	7.0-8.2	0.04	0.03	0.03	0.02	0.01	0.01	0.01	0.01	1
pCO2 [μatm]	250-550	46								2

1402